Astrocytic Neurexin-1 Orchestrates Functional Synapse Assembly

Justin H. Trotter[1,*,#], Zahra Dargaei[1,*], Markus Wöhr[1,&], Kif Liakath-Ali[1], Karthik Raju[1], Sofia Essayan-Perez[1], Amber Nabet[1], Xinran Liu[2], and Thomas C. Südhof[1,3,#]

[1]Dept. of Molecular and Cellular Physiology, Stanford University School of Medicine, Stanford, CA 94305, USA; [2]Department of Cell Biology, Yale University School of Medicine, New Haven, CT 06510; [3]Howard Hughes Medical Institute, Stanford University School of Medicine, Stanford, CA 94305, USA.

*These authors contributed equally to the study

[&]Present addresses: Laboratory for Behavioral Neuroscience, Department of Biology, Faculty of Science, University of Southern Denmark, Campusvej 55, DK-5230 Odense M, Denmark, and Behavioral Neuroscience, Experimental and Biological Psychology, Faculty of Psychology, Philipps-University of Marburg, Gutenbergstraße 18, D-35032 Marburg, Germany.

[#]Address for correspondence (justint3@stanford.edu; tcs1@stanford.edu)

ABSTRACT

At tripartite synapses, astrocytes surround synaptic contacts, but how astrocytes contribute to the assembly and function of synapses remains unclear. Here we show that neurexin-1α, a presynaptic adhesion molecule that controls synapse properties, is also abundantly expressed by astrocytes. Strikingly, astrocytic neurexin-1α, but not neuronal neurexin-1α, is highly modified by heparan sulfate. Moreover, astrocytic neurexin-1α is uniquely alternatively spliced and invariably contains an insert in splice-site #4, thereby restricting the range of ligands to which it binds. Deletion of neurexin-1 from astrocytes or neurons does not alter synapse numbers or synapse ultrastructure, but differentially impairs synapse function. At hippocampal Schaffer-collateral synapses, neuronal neurexin-1 is essential for normal NMDA-receptor-mediated synaptic responses, whereas astrocytic neurexin-1 is required for normal AMPA-receptor-mediated synaptic responses and for long-term potentiation of these responses. Thus, astrocytes directly shape synapse properties via a neurexin-1-dependent mechanism that involves a specific molecular program distinct from that of neuronal neurexin-1.

INTRODUCTION

Many synapses in the brain are tripartite owing to their physical proximity to astrocytic processes (Kikuchi et al., 2020; Ventura and Harris, 1999; Papouin et al., 2017; Durkee and Araque, 2019). Although several important astrocytic proteins that promote synapse formation have been identified (e.g. SPARCL1, thrombospondin-1, Chordin-like 1, TGFβ, and glypicans), the molecular mechanisms utilized by astrocytes to instruct synapse formation and to regulate synapse function are largely unknown (Allen et al., 2012; Blanco-Suarez et al., 2018; Christopherson et al., 2005; Diniz et al., 2012; Kucukdereli et al., 2011; Nagal et al., 2019). Recent studies have implicated cell-adhesion molecules expressed by astrocytes, such as neuroligins and Ephrin-B1, in regulating synapse formation (Koeppen et al., 2018; Stogsdill et al., 2019). However, the extent to which astrocytes employ these or other cell adhesion molecules to regulate synaptic information processing remains unclear (Bohmback et al., 2018; Durkee et al., 2019; Farhy-Tsenlnicker et al., 2018; Papouin et al., 2017). Interestingly, single-cell RNAseq data show particularly high levels of the presynaptic cell-adhesion molecule neurexin-1 (Nrxn1) in astrocytes (Fig. S1), suggestive of a non-neuronal function of Nrxn1. Whether the expression of Nrxn1 in astrocytes is physiologically significant and whether astrocytes contribute to synaptic transmission via a Nrxn1-dependent pathway has not been examined. Importantly, copy number variations (CNVs) that selectively alter expression of Nrxn1 (encoded by the *NRXN1* gene in humans) are among the most frequent single-gene mutations observed in patients with schizophrenia, Tourette syndrome, autism, and other neurodevelopmental disorders (reviewed in Kasem et al., 2018; Südhof, 2017), suggesting that heterozygous loss-of-function of *NRXN1* predisposes to neuropsychiatric diseases. Given that astrocyte dysfunction has also been implicated in neuropsychiatric disorders (Dietz et al., 2020; Nagai et al., 2019; Perez et al., 2020), determining the role of Nrxn1 in astrocytes thus is crucial for insight into how *NRXN1* mutations predispose to disease.

Neurexins are encoded by three genes that direct synthesis of longer α-neurexins and shorter β-neurexins via distinct promoters (Ushkaryov et al., 1992, 1994; Ushkaryov and Südhof, 1993). Extracellularly, α-neurexins possess six laminin/neurexin/sex hormone–binding globulin (LNS) domains that are interspersed with EGF-like repeats. In contrast, β-neurexins contain a short β-specific N-terminal sequence that splices into the α-neurexin

sequence upstream of their sixth LNS domain. Following the sixth LNS domain, neurexins include a glycosylated “stalk” region that includes a site for heparan sulfate modification (Zhang et al., 2018), a cysteine-loop domain, a transmembrane region, and a cytoplasmic tail. The neurexin-1 gene (*Nrxn1*) additionally encodes a third isoform called neurexin-1γ (Nrxn1γ) that lacks LNS domains (Sterky et al., 2017; Yan et al., 2015). Neurexin mRNAs are extensively alternatively spliced at six canonical sites producing thousands of isoforms (Schreiner et al., 2014; Treutlein et al., 2014; Ullrich et al., 1995) that are differentially expressed by neuronal subclasses (Fuccillo et al., 2015; Lukacsovich et al., 2019). Presynaptic neurexins concentrate in nanoclusters (Trotter et al., 2019) that interact trans-synaptically with a panoply of postsynaptic ligands. These ligands include neuroligins, secreted cerebellins complexed with GluD1 or GluD2, leucine-rich repeat transmembrane proteins (LRRTMs), dystroglycan, and calsyntenin-3 (reviewed in Roppongi et al., 2017; Südhof, 2017; Yuzaki, 2017). Many neurexin interactions are modulated by alternative splicing, including those of LRRTMs (Ko et al., 2009; Siddiqui et al., 2010), cerebellins (Joo et al., 2011; Matsuda and Yuzaki, 2011; Uemura et al., 2010), and neuroligins (Boucard et al., 2005; Chih et al., 2006; Comoletti et al., 2006; Elegheert et al., 2017; Ichtchenko et al., 1995). By virtue of their transsynaptic interactions, neurexins specify diverse synaptic properties. For example, neurexins regulate presynaptic Ca^{2+} channels (Chen et al., 2017; Luo et al., 2020; Missler et al., 2003), postsynaptic tonic endocannabinoid synthesis (Anderson et al., 2015), and postsynaptic AMPA- (AMPARs) and NMDA-receptors (NMDARs) (Aoto et al., 2013; Dai et al., 2019).

Currently it is unclear whether astrocytic Nrxn1 is required for synapse development or function, and if so, how the function of astrocytic Nrxn1 differs from that of neuronal Nrxn1, perhaps by simultaneously communicating via a shared repertoire of postsynaptic ligands. Here, we show that astrocytic and neuronal Nrxn1 fundamentally differ in the expression of major isoforms, patterns of mRNA alternative splicing, and post-translational heparan sulfate modification. Consistent with these differences, we found that astrocytic and neuronal Nrxn1 exhibit distinct ligand binding properties and perform different roles in specifying hippocampal excitatory synapse properties. In particular, we observed that loss of Nrxn1 in astrocytes impaired postsynaptic AMPAR strength, long-term synaptic plasticity and mouse behavior, consistent with the role of Nrxn1 CNVs in the etiology of neurodevelopmental disorders. Taken together, our results reveal an unexpected

molecular choreography by which astrocytic and neuronal Nrxn1 collaborate to organize synapse properties.

RESULTS

Astrocytes and neurons express Nrxn1α at equivalent levels. Using single-molecule RNA *in situ* hybridization, we observed *Nrxn1* expression both in neurons and astrocytes (Figure 1A, S2A). To quantify the levels of *Nrxn1* mRNAs in neurons and astrocytes, we crossed Cre-dependent 'RiboTag' mice (Sanz et al., 2009) with Cre-driver mouse lines that express Cre only in neurons (Baf53b-Cre) or astrocytes (Aldh1l1-CreERT2, induced with tamoxifen). We validated the cell type-specific expression of Cre in these driver lines using a reporter mouse line, which revealed no detectable spillover of Cre expression in other cell types (Fig. S2B, S2C). We then purified ribosome-bound mRNAs from neurons or astrocytes in the Cre-driven RiboTag mice and validated the specificity of the mRNA purification by quantitative RT-PCR of marker genes (Fig. S2D). Using the same mRNAs, we measured the relative mRNA levels of *Nrxn1α* and of other neurexins in astrocytes and neurons (Fig. 1B). *Nrxn1α* and *Nrxn2* mRNAs were abundant in astrocytes and neurons, whereas other neurexin mRNAs were enriched in neurons and de-enriched in astrocytes.

Although the mRNA measurements by *in situ* hybridization and qRT-PCR confirm high-level expression of *Nrxn1α* in astrocytes, absolute expression levels are difficult to ascertain from such measurements due to technical limitations (Fig. 1A, 1B), as is also apparent from the differences between various single-cell RNAseq studies (Fig. S1). To directly measure the amounts of Nrxn1 protein in astrocytes or neurons, we crossed *Nrxn1* conditional KO (cKO) mice (Trotter et al., 2019; Chen et al., 2017) with the neuron- and astrocyte-specific Cre-driver mice described above, resulting in mice with neuron- or astrocyte-specific deletions of *Nrxn1* (referred to, respectively, as 'neuron cKO' and 'astrocyte cKO' mice). In addition, we crossed *Nrxn1* cKO mice with Nestin Cre-driver mice to delete *Nrxn1* from the entire brain (referred to as 'brain cKO'; Fig. 1C-1E). Brain, neuron, and astrocyte *Nrxn1* cKO mice survived normally into adulthood, but brain and neuron *Nrxn1* cKO mice exhibited reduced body weights (Fig. 1F-1H). Analyses of the protein levels of Nrxn1α (the major Nrxn1 isoform) showed that the neuron and the

astrocyte *Nrxn1* cKO each have decreased amounts of total Nrxn1α protein by approximately 50%, whereas the brain *Nrxn1* cKO ablated nearly all Nrxn1α (Figure 1I-1L). Detection of pan-α-neurexin levels using antibodies against the conserved C-terminus of neurexins revealed considerable reductions in pan-α-neurexin levels in brain, neuron, and astrocyte *Nrxn1* cKOs mice (Figure 1I-1L, S2E). Consistent with neuron-specific enrichment of *Nrxn1*β mRNAs (Figure 1B), deletion of *Nrxn1* in the brain and in neurons, but not astrocytes, resulted in a 50% decrease in pan-β-neurexin protein levels (Figure 1I-L, S2E). Thus, astrocytes and neurons produce similar amounts of Nrxn1α protein in brain, while only neurons express Nrxn1β protein.

To further confirm the contribution of neurons and astrocytes to Nrxn1 protein levels, we used conditional knock-in mice in which an HA-epitope is inserted into the 'stalk' sequence of Nrxn1 (Fig. S3A; Trotter et al., 2019). In these mice, the last exon of the *Nrxn1* gene is additionally flanked by loxP sites. As a result, Cre recombination of the conditional HA-knockin *Nrxn1* gene deletes the last exon that encodes the Nrxn1 transmembrane region and causes production of a truncated, non-functional secreted Nrxn1 fragment, prompting us to refer to the Cre recombinase-induced state in these mice as conditional KO-truncation (cKO-T). Because in the *Nrxn1* HA-knockin mice endogenous Nrxn1 is HA-tagged in the absence of Cre-recombinase, these mice enable accurate and sensitive analyses of Nrxn1 protein that would not be possible with available antibodies to Nrxn1 (Trotter et al., 2019). After crossing these mice to brain, neuron, and astrocyte Cre driver mice, we found that neuron and astrocyte HA-Nrxn1 cKO-T mice both had ~35-50% reductions in Nrxn1α protein levels (Fig. S3B-S3D). Consistent with cell-specific enrichment of *Nrxn1* mRNAs (Fig. 1B) and with the Nrxn1 protein quantifications in cKO mice (Fig. 1I-1L, S2E), Nrxn1β and Nrxn1γ protein levels were nearly abolished in brain and neuron cKO-T mice but unchanged in astrocyte cKO-T mice (Fig. S3B-S3D).

Nrxn1 is localized on astrocytic processes in the neuropil. The *Nrxn1* HA-knockin mice permit specific analyses of the localization of endogenous Nrxn1 using HA antibodies (Fig. S3E, S3F; Trotter et al., 2019). We first analyzed the localization of HA-Nrxn1 in astrocytes using both mixed neuron-glia cultures and astrocyte-enriched glia cultures (Fig. 2A). Different from the analysis of HA-Nrxn1 localization of brain sections (see below), we could examine in these experiments the surface localization of Nrxn1 by analyzing non-

permeabilized cells. Nrxn1 was present in a largely punctate pattern blanketing the entire surface of astrocytes, consistent with a localization to specific plasma membrane domains (Fig. 2A, S3E-S3F).

We next evaluated the distribution of astrocytic Nrxn1 in the brain by crossing the HA-Nrxn1 cKI mice to brain and astrocyte Cre driver mice. In the hippocampus and cortex of HA-Nrxn1 brain cKO-T mice we observed a decrease in Nrxn1 staining in the neuropil and reduced but still detectable staining in the somas of both neurons and astrocytes (Fig. S3G, S3H). In hippocampal sections from HA-Nrxn1 astrocyte cKO-T mice, we observed a profound reduction in Nrxn1 levels throughout synaptic subfields, suggesting that Nrxn1 localizes to astrocyte processes in the neuropil (Fig. 2B). Sparse deletion of Nrxn1 via AAV-mediated expression of Cre in astrocytes revealed a major reduction in Nrxn1 staining in the neuropil, with higher magnification images suggesting that a robust fraction of the Nrxn1 staining in the neuropil is due to astrocytic Nrxn1 (Fig. 2C). Although the specific localization of Nrxn1 cannot be examined in these sections owing to the detection of both intracellular and surface-exposed Nrxn1, these data do support the results obtained in cultured astrocytes suggesting that Nrxn1 is expressed uniformly on all astrocytic processes.

Nrxn1α is highly heparan sulfate modified in astrocytes but not in neurons. Nrxn1 is highly glycosylated (Ushkaryov et al., 1992) and additionally modified by heparan sulfate, which has been implicated in controlling ligand binding and synapse formation (Roppongi et al., 2020; Zhang et al., 2018). To determine whether Nrxn1α exhibits different molecular properties in astrocytes and neurons, we performed immunoblotting analyses of Nrxn1α in cultures composed of only glia that were enriched for astrocytes or of glia mixed with neurons (Fig. 3A). Strikingly, Nrxn1α in glia was present at a much higher molecular weight than in cultures with neurons (Fig. 3A). Since modification by heparan sulfate dramatically increases the apparent molecular weight of Nrxn1α (Zhang et al., 2018), we tested the effect of heparinases on Nrxn1α. Heparinases selectively remove heparan sulfate modifications, and the remaining ‘stubs’ can be quantified with specific antibodies (David et al., 1992). Heparinase treatment of Nrxn1α immunoprecipitated from glia cultures caused a shift of nearly all Nrxn1α protein to a lower molecular weight, whereas the same treatment of Nrxn1α immunoprecipitated from mixed neuron and glia cultures

produced only a shift of the higher-molecular weight forms of Nrxn1α (Fig. 3A-3B). Quantifications of the heparan sulfate 'stubs' remaining after heparinase treatment demonstrated that Nrxn1α derived from glia is almost completely modified by heparan sulfate, whereas Nrxn1α derived from mixed neuron-glia cultures is only partly modified by heparan sulfate (Fig. 3A, 3C). These results indicate that Nrxn1α is preferentially, if not exclusively, expressed as a heparan sulfate proteoglycan in astrocytes but not in neurons. To validate this conclusion, we analyzed the migration pattern of Nrxn1α, as well as other Nrxn1 isoforms, from the lysate of brain, neuron, and astrocyte cKO-T and littermate control mice. We found that Nrxn1α comprises ~80% of total Nrxn1 protein levels, with neuron-specific Nrxn1β and Nrxn1γ isoforms expressed at substantially lower levels (Fig. 3E). Similar to Nrxn1α, Nrxn1β and Nrxn1γ were also present in highly modified forms, probably because they are also subject to heparan sulfate modifications (Fig. 3E).

Since astrocytes only express Nrxn1α, we compared the migration pattern of Nrxn1α in neuron and astrocyte cKO-T brain lysates. Under control conditions, native brain Nrxn1α migrated on SDS-gels as a heterogeneous set of bands with a diffuse high-molecular weight component (Fig. 3F, S4A). We next immunoprecipitated Nrxn1α from the brain of the control and neuron and astrocyte cKO-T mice, treated the immunoprecipitated Nrxn1α with heparinases, and analyzed Nrxn1α by immunoblotting for HA-Nrxn1 and for heparan sulfate stubs (Fig. 3F-3H). Deletion of Nrxn1 from neurons did not alter the diffuse high-molecular weight component and selectively decreased the intensity of the lower bands, whereas deletion of Nrxn1 from astrocytes nearly eliminated the high-molecular weight bands (Fig. 3F, 3G, S4A). Moreover, deletion of Nrxn1 from neurons had a minor effect on the levels of heparan sulfate-modified Nrxn1α after heparinase treatment, whereas deletion of Nrxn1 from astrocytes almost completely eliminated the presence of heparan sulfate-modified Nrxn1α stubs (Fig. 3F, 3H). Thus, astrocytic Nrxn1α is highly modified by heparan sulfate and in the brain heparan sulfate modification of Nrxn1α is almost exclusive to astrocytes.

Neurons and astrocytes differ in Nrxn1 mRNA alternative splicing. Alternative splicing of neurexin mRNAs provides neurons with a molecular switch for specifying ligand binding and tuning synaptic properties (reviewed in Südhof, 2018). Since astrocytic and neuronal

Nrxn1 may converge upon similar postsynaptic structures and share access to ligands, differential alternative splicing of *Nrxn1* mRNAs represents a powerful potential mechanism to direct information flow between different compartments of the tripartite synapse. To address this possibility, we determined whether alternative splicing of *Nrxn1* mRNAs differs between neurons and astrocytes. First, we compared *Nrxn1* splicing in astrocyte-enriched glial cultures to mixed cultures containing both neurons and glia. We observed striking differences in alternative splicing, such as exclusive expression of *Nrxn1* mRNAs containing splice insert #4 and lacking #6 in cultured glia (Fig. 4A-4B). This comparison, however, has limitations because mixed cultures also contain glia, glial cultures are not purely comprised of astrocytes, and *in vitro* conditions might not faithfully recapitulate *Nrxn1* mRNA splicing patterns in the brain. Therefore, we compared *Nrxn1* mRNA alternative splicing in neurons and astrocytes from brain tissue using mRNA isolated via RiboTag pulldowns (described in Fig. 1B, S2D). Mirroring our findings in cultured glia (Fig. 4A, 4B), astrocytic *Nrxn1* mRNA displayed strikingly more restricted patterns of alternative splicing than neuronal *Nrxn1* mRNA (Fig. 4C-4H). In particular, astrocytic *Nrxn1* mRNA nearly always lacked inserts in splice sites #1, #2, and #6, but contained an insert in splice site #4, whereas in neurons *Nrxn1* mRNAs were much more heterogeneously alternatively spliced (Fig. 4C-4H).

Nrxn1 expressed by neurons and astrocytes differ in ligand binding. In the heterologous synapse formation assay, neurexin ligands (e.g. neuroligins) expressed on the surface of non-neuronal cells (e.g. COS or HEK293T cells) cluster neurexins on the surface of co-cultured neurons and induce formation of presynaptic specializations on these neurons (Graf et al., 2004; Nam and Chen, 2005; Scheiffele et al., 2000). We modified this assay using cultures of mixed hippocampal neurons and glia or astrocyte-enriched glia to screen ligands for their ability to bind to endogenous Nrxn1. Using cultures of mixed hippocampal neurons and glia from *Nrxn1* HA-knockin mice, we first verified that a panel of established neurexin ligands expressed on the surface of HEK293T cells readily clustered surface Nrxn1 and recruited presynaptic terminals (Fig. S4C, S4D). Since differences in Nrxn1 heparan sulfate modification (Fig. 3, S4A, S4B) and mRNA splicing (Fig. 4A-4H) were preserved in cultured glia compared to astrocytes *in vivo*, we next determined whether neurexin ligands overexpressed on the surface of HEK293T cells could cluster endogenous Nrxn1 on the surface of astrocytes in glia cultures (Fig. 4I-4J).

We found that only a subset of ligands could cluster astrocytic Nrxn1, demonstrating that astrocytic Nrxn1 can form transcellular complexes, and that the molecular differences between Nrxn1 expressed by neurons and astrocytes confer ligand specificity.

Specifically, we found that astrocytic Nrxn1 interacted with a membrane-anchored chimeric variant of neurexophilin-1, neuroligin-1 lacking the splice site B insert (-SSB), and cerebellin-1 complexed with GluD1 (Fig. 4I-4J). Unlike in mixed cultures, heparinase treatments of glia had no major effect on the ability of neurexin ligands to cluster surface Nrxn1 on astrocytes, suggesting that the heparan sulfate modification of astrocytic Nrxn1 is not required for binding ligands screened in this assay (Fig. S4E, S4F).

Deletion of Nrxn1 in astrocytes and neurons causes distinct gene expression changes. To determine whether neuronal or astrocytic Nrxn1-mediated signaling regulates global patterns of gene transcription, we performed bulk RNAseq experiments on hippocampal tissue from mice with astrocyte- or neuron-specific *Nrxn1* deletions (Fig. 5). Both deletions caused significant gene expression changes, but the pattern of differentially expressed genes differed, with no overlap except for *Nrxn1* itself (Fig. 5A). The neuron-specific *Nrxn1* deletion increased expression of a protein involved in regulating AMPA-receptors (Nptx2; O'Brien et al., 1999) and two signal transduction proteins (Gigyf1 and Gnb2), and decreased expression of two proteins involved in trans-synaptic cell adhesion (Syndig1 and C1ql3; Kalashnikova et al., 2010; Matsuda et al., 2016). The astrocyte-specific *Nrxn1* deletion, conversely, caused a highly significant upregulation of lipoprotein lipase, as well as a component of perineural nets (Hapln4; Bekku et al, 2003) and intercellular junctions (Ocel1), and a downregulation of the transporter Slc5a5 (Fig. 5A). Quantitative RT-PCR confirmed the most significant gene expression changes (Fig. 5B-5C). Hence, deletion of *Nrxn1* in neurons versus astrocytes produces profound but distinct changes in brain gene expression.

Deletion of Nrxn1 from astrocytes impairs spontaneous synaptic events without affecting synapse numbers. We next asked whether the neuronal or astrocytic deletion of *Nrxn1* alters synapse numbers, motivated by reports suggesting that the heparan sulfate modification of Nrxn1 is important for synapse formation (Zhang et al., 2018). Using acute slices from young mice with brain-, neuron-, and astrocyte-specific *Nrxn1* deletions, we measured spontaneous miniature excitatory postsynaptic currents (mEPSCs) in CA1

pyramidal neurons. Strikingly, we observed a large decrease in mEPSC frequency following brain-specific (~35%) and astrocyte-specific *Nrxn1* deletions (~55%), but not after neuron-specific *Nrxn1* deletions (Fig. 6A-6C). The mEPSC amplitude and kinetics were unchanged, as were basic membrane properties (Fig. 6A-C, S5A-S5O).

The decrease in mEPSC frequency induced by deletion of *Nrxn1* from astrocytes could be caused, among others, by a decrease in synapse numbers. However, when we measured the synapse density in different layers of the CA1 region by immunohistochemistry for the excitatory presynaptic marker vGluT1 (Fig. 6D-6I, S6A) or directly by electron microscopy (Fig. 6J-6K), we observed no change in excitatory synapse density. Moreover, we found no change in excitatory synapse density in the CA3 region after brain-specific deletion of *Nrxn1* (Fig. S6B), contradicting a previous report that heparan sulfate modification of Nrxn1 regulates excitatory synapse formation in this region (Zhang et al., 2018). We also did not observe a change in inhibitory synapse density in the CA1 region (Fig. S6C). Furthermore, electron microscopy revealed no significant change in ultrastructural parameters of synapses, suggesting that the astrocytic *Nrxn1* cKO does not alter synapse structure (Fig. 6J-6K, S6D). Finally, we found no significant alteration in the levels of synaptic proteins in the hippocampus (Fig. S6E). Viewed together, these experiments indicate that deletion of *Nrxn1* in neurons or astrocytes does not alter synapse numbers.

Nrxn1 mediates distinct synaptic functions in astrocytes and neurons. An alternative explanation for the decreased mEPSC frequency observed after astrocyte-specific deletions of *Nrxn1* (Fig. 6C) is a decrease in synaptic transmission rather than synapse numbers. To explore this possibility, we monitored AMPAR- and NMDAR-mediated synaptic responses in acute slices obtained from brain-, neuron- and astrocyte-specific *Nrxn1* cKO mice. Using whole-cell patch-clamp recordings, we found that the brain- and neuron-specific *Nrxn1* cKO both significantly decreased the NMDAR/AMPAR ratio, whereas surprisingly the astrocyte-specific cKO increased the NMDAR/AMPAR ratio (Fig. 7A, 7D, 7G). Next, we measured the strength of AMPAR- and NMDAR-mediated synaptic transmission separately, using input-output curves to control for differences in action potential generation. The brain cKO of *Nrxn1* decreased the strength of both AMPAR- and NMDAR-mediated synaptic transmission (Fig. 7B, 7C), the neuron-specific cKO of *Nrxn1* decreased only the strength of NMDAR-mediated synaptic transmission (Fig. 7E, 7F), and

the astrocyte-specific cKO of *Nrxn1* decreased only the strength of AMPAR-mediated synaptic transmission (Fig. 7H, 7I). The decrease in NMDA- and AMPAR-mediated synaptic transmission induced by *Nrxn1* deletions in neurons and astrocytes, respectively, was not due to a decrease in release probability, because the paired-pulse ratio was unchanged (Fig. S5P, S5Q). Moreover, the astrocyte-specific, but not the neuron-specific *Nrxn1* deletion impaired long-term potentiation (Fig. 7J, 7K). Thus, deletion of *Nrxn1* in neurons and astrocytes profoundly and differentially impaired synaptic transmission and plasticity.

Nrxn1 deletion in astrocytes perturbs sensory pre-pulse inhibition. Given the distinct functions of *Nrxn1* in neurons versus astrocytes, we asked whether astrocyte-specific *Nrxn1* deletions cause behavioral impairments. Using age- and sex-matched littermate mice, we found that most behavioral parameters are unaffected by the astrocytic deletion of *Nrxn1* (Fig. 7L-7N, S7). The deletion caused no significant changes in open field behavior, working memory as measured using the Y-maze, nest building, self-grooming, or fear conditioning except for a minor decrease in long-term memory (Fig. S7Q). However, astrocyte-specific deletion of *Nrxn1* did result in slightly abnormal motor coordination in a standard rotarod task (Fig. S7F) and a significant increase in fur lesions (Fig. S7I). Most notably, the astrocyte-specific deletion of *Nrxn1* significantly impaired the pre-pulse inhibition of the startle response (Fig. 7L-7N), a behavioral change that is characteristically observed in patients with schizophrenia (DiLalla et al., 2017; Javitt et al., 2015). Whereas the acoustic startle response itself was normal (Fig. 7L), pre-pulse inhibition of the startle response was impaired (Fig. 7M, 7N).

DISUCSSION

In this study, we demonstrate that astrocytes express high levels of Nrxn1α, a presynaptic cell-adhesion molecule that is unlike any protein studied in astrocytes to date owing to its unique ability to communicate with synapses via a rich diversity of synaptic ligands. Although many astrocyte factors have been found to promote synaptogenesis, only a few prior studies have addressed how astrocytes regulate synaptic function. Here, we describe an unexpected molecular choreography between astrocytes and neurons involving the expression of Nrxn1α variants that differ in alternative splicing and heparan sulfate

modification. Owing to their molecular differences, neuronal and astrocytic Nrxn1 displayed unique ligand binding profiles and regulated distinct functional features of excitatory synapses without affecting synapse numbers. In particular, we found that deletion of *Nrxn1* in astrocytes impaired AMPAR-mediated synaptic transmission and long-term synaptic plasticity, while deletion of *Nrxn1* in neurons impaired NMDAR-mediated synaptic transmission. Furthermore, deletion of *Nrxn1* in astrocytes disrupted a common measure of sensorimotor gating, pre-pulse inhibition, which is of interest given that such an impairment represents a characteristic endophenotype of schizophrenia (DiLalla et al., 2017; Javitt et al., 2015) and that *NRXN1* mutations represent the most common single-gene mutations in schizophrenia (Hu et al., 2019; Marshall et al., 2017; Rees et al., 2014).

Previously, it was found that constitutive deletion of Nrxn1 impairs AMPAR-mediated synaptic transmission in CA1 pyramidal neurons (Etherton et al., 2009). Although a role for astrocytic Nrxn1 was not considered at the time, results from this study are consistent with the present finding that astrocytic deletion of Nrxn1, which is expressed exclusively as the Nrxn1α isoform (Fig. 1, S2E, S3D), selectively impairs AMPAR responses (Fig. 7). Considering that NMDAR responses are normal in Nrxn1α KO mice (Etherton et al., 2009), our finding that NMDAR responses are impaired following *Nrxn1* deletion in neurons (Fig. 7) suggests that Nrxn1β may contribute to regulating NMDAR responses at this synapse. An important consideration is that astrocytic and neuronal *Nrxn1* may behave differently at other synapses in the hippocampus and beyond. Indeed, at a neighboring synapse formed between CA1 projection neurons and target cells in the subiculum, individual presynaptic Nrxns regulate distinct functions, including regulation of NMDAR responses by Nrxn1 (Dai et al., 2019), AMPAR responses by Nrxn3 (Aoto et al., 2013), and the presynaptic release probability and tonic endocannabinoid synthesis by β-neurexins (Anderson et al., 2015). Similar to presynaptic neurexins, astrocytic Nrxn1 may not have a universal function in regulating AMPAR-mediated transmission, but rather, its function may be context-dependent. Moreover, expression of Nrxn2 by astrocytes (Fig. 1B) may play a role in additional functions or compensate in the absence of Nrxn1, thus obscuring additional functions that went undetected when we deleted *Nrxn1* in astrocytes.

A previous study found that astrocytic expression of neuroligins, a family of well-characterized postsynaptic ligands of neurexins, regulates astrocyte morphogenesis and

synapse formation in the developing visual cortex (Stogsdill et al., 2017). It is important to note several limitations of this work and differences from our study. Limitations include the use of sparse manipulations that can cause artifacts, which might not occur in global KO mice, as observed in sparse versus global manipulations of neuronal neuroligins (Kwon et al., 2012). Other limitations are the use of shRNA-mediated knockdowns that frequently give rise to off-target effects, and the use of GLAST-CreERT2 driver mice that exhibit poor recombination efficiency and targeting of forebrain astrocytes (Srinivasan et al., 2016; Yu et al., 2020). Moreover, the absence of major changes in excitatory synapse formation in cultures and tissue from neuroligin constitutive KO mice (Poulopoulos et al., 2009; Chubykin et al., 2007; Varoqueaux et al., 2006) implies that the proposed role of astrocytic neuroligins in synapse formation is not a universal function. In contrast, in our study, we systematically employed mouse genetics to profile the molecular and functional characteristics of Nrxn1 in neurons and astrocytes. Unlike the previous study, where the relative amount of astrocytic versus neuronal neuroligins was unclear (Stogsdill et al., 2017), we show strong evidence that astrocytic Nrxn1α constitutes a significant and molecularly distinct population of Nrxn1α protein in the hippocampus. Furthermore, we demonstrate that presynaptic and astrocytic Nrxn1 differentially shape the properties but not numbers of excitatory synapses in hippocampal area CA1. We utilized multiple complementary approaches to measure synapse numbers including immunostaining, immunoblotting and electron microscopy. Finally, technical limitations of the previous study aside, a universal function of neuroligins in regulating excitatory synapse formation and astrocyte morphogenesis is an exciting proposition and would suggest that they could compete, in *cis*, with astrocytic neurexins. However, the phenotype we have observed following astrocyte-specific deletion of Nrxn1 is incompatible with this notion, as we do not see a change in synapse number in either direction, but instead, observe impaired synaptic transmission. It remains possible that astrocytic neuroligins in the hippocampus do not act in a manner similar to their described role in the developing visual cortex (Stogsdill et al., 2017) or that they are spatially or temporally segregated from neurexins so as to prevent competition.

Our findings raise the tantalizing possibility that astrocytic Nrxn1α traffics to astrocyte-synapse junctions within tripartite synapses. This notion is suggested by the presence of

dense astrocytic Nrxn1 puncta throughout the entire territory of hippocampal astrocytes, including fine processes that invade the neuropil (Fig. 2B-2C), the ability of a subset of postsynaptic ligands to cluster astrocytic Nrxn1 when presented in *trans* (Fig. 4I), and the pronounced effect of astrocytic Nrxn1 on the properties of CA1 excitatory synapses (Fig. 6C, 7) that frequently contain an astrocytic component (Ventura and Harris, 1999). If indeed both presynaptic and astrocytic Nrxn1 are in proximity to postsynaptic structures, differences in Nrxn1 mRNA alternative splicing or heparan sulfate modification of Nrxn1 may confer ligand specificity, thereby segregating the flow of information from astrocytic and presynaptic Nrxn1. For example, astrocytic Nrxn1 transcripts almost exclusively include splice site #4, which might serve to accommodate binding to the only known SS#4^{+}-specific interactors, cerebellins (Uemura et al., 2010). Supporting this notion, we demonstrate that astrocytic Nrxn1 could be clustered by cerebellin-1/GluD1 but not LRRTM2 (Fig. 4I-J). However, the absence of an AMPAR phenotype following CA1-specific deletion of GluD1 (Liu et al., 2020) suggests that an interaction between cerebellins and astrocytic Nrxn1 does not readily explain why astrocytic *Nrxn1* primarily includes SS#4. Alternatively, the inclusion of splice site #4 in astrocytic Nrxn1α may prevent interactions that could otherwise promote inappropriate stabilization of glutamate receptors to the perisynaptic membrane as might be caused by LRRTMs (Aoto et al., 2013; Bhouri et al., 2018).

Importantly, our study further demonstrates that astrocytic Nrxn1α is a major heparan sulfate proteoglycan of the brain. However, our results disagree with an earlier study showing the heparan sulfate modification of synaptic Nrxn1 regulates excitatory synapse formation (Zhang et al., 2018) in two ways. First, we found that *Nrxn1* deletions in the entire brain via Nestin Cre did not alter excitatory synapse numbers in the CA1 and CA3 regions, the latter of which is the region studied by Zhang et al. (2018). Second, we found that astrocytic Nrxn1α is preferentially heparan sulfate modified while neuronal Nrxn1α is almost completely unmodified (Fig. 3). We did, however, observe that neurons express Nrxn1β and Nrxn1γ proteins both with and without heparan sulfate modifications (Fig. 3D, 3F). Since our *Nrxn1* cKO mice do not target Nrxn1γ, it remains possible that in our mice this neuron-specific isoform can compensate thus allowing normal excitatory synapse formation, as has been recently suggested (Roppongi et al., 2020). Because we found that

the heparan sulfate modification of astrocytic Nrxn1 is dispensable for binding to a subset of ligands (Fig. S4F), it prompts us to ask what is the functional importance of this modification? One possibility is that the heparan sulfate modification enables or regulates the affinity of an untested but known ligand (e.g. other neuroligins or LRRTM3/LRRTM4 that were recently identified as heparan sulfate ligands (Roppongi et al., 2020)). Alternatively, the heparan sulfate modification by itself may facilitate an unknown interaction with heparan sulfate binding proteins such as pleiotrophin, f-spondin, or others (Zhang et al., 2018). The comparative lack of the heparan sulfate modification in neurons challenges the view that the heparan sulfate moiety itself is a fundamental positive regulator of neurexin function and raises interesting questions on the very mechanisms responsible for different levels of the Nrxn1α heparan sulfate modification in astrocytes and neurons. Potentially explaining why neurons, unlike astrocytes, maintain a large pool of non-heparan sulfate modified Nrxn1, we recently found that FAM19A proteins act as neuron-specific, pan-neurexin ligands and bind to the conserved Cys-loop domain of neurexins in the secretory pathway thereby preventing addition of heparan sulfate (Khalaj et al., 2020).

Taken together, our findings reveal that astrocytes modulate synaptic function via a neurexin-dependent mechanism that differs from the mechanism of action of neuronal neurexins in synapse specification and suggest that dysfunctional astrocyte-synapse communication may contribute to neuropsychiatric disorders. Several major questions arise at this juncture. Do astrocytes express functionally relevant levels of Nrxn2, and does astrocytic Nrxn2 functionally overlap with astrocytic Nrxn1? Moreover, does astrocytic Nrxn1 traffic to the point of contact between astrocytic and synaptic membranes, and if so, what ligands does it interact with? Furthermore, what are the functional consequences of key molecular features of astrocytic Nrxn1, including its heparan sulfate modification and alterative splicing? Finally, do astrocytic neurexins and neuroligins cooperate or compete to interact with synapses or are they trafficked to unique subcellular compartments of astrocytic processes? Addressing these questions will further advance our understanding of how astrocytes regulate synapses beyond the present discovery that such regulation is mediated in a specific manner by molecularly distinct astrocytic Nrxn1α variants.

STAR METHODS

EXPERIMENTAL MODEL AND SUBJECT DETAILS

Mouse Generation and Husbandry. *Nrxn1* conditional KO (cKO) and *Nrxn1* HA-knockin mice were generated as described previously (Chen et al., 2017; Trotter et al., 2019). Other mouse lines used in this paper include Nestin-Cre (Jax, stock# 003771), BAF53b-Cre (Jax, stock# 027826), Aldh1l1-CreERT2 (Jax, stock# 029655), Ai14 tdTomato Cre reporter (Jax, stock# 007914), Ai75D tdTomato Cre reporter (Jax, stock# 025106), and RiboTag mice (Jax, stock# 029977). Breeding strategies (Fig. 1) were designed to ensure that Cre and reporter alleles, when present, were hemizygous. Weight and survival of *Nrxn1* brain, neuron, and astrocyte cKOs was evaluated at post-natal day 21 (P21). Wild-type CD-1 mice were used as control animals for a subset of immunostaining, RNA localization, and biochemical experiments. All mice were weaned at 20 days of age and housed in groups of 2-5 on a 12 hr light/dark cycle with access to food and water *ad libidum*. All procedures conformed to National Institutes of Health Guidelines for the Care and Use of Laboratory Mice and were approved by the Stanford University Administrative Panel on Laboratory Animal Care.

Mixed Hippocampal Neuron-Glia Cultures. Hippocampal cultures containing neurons and glia (i.e., mixed) were generated from P0 *Nrxn1* HA-knockin mice (Fig. 2, 3, S3, and S4) or wild-type CD-1 mice (Fig. 4). Hippocampi were dissected and mixed regardless of gender. In general, pooling tissue from three to six mice, in a given preparation was used to generate cultures. Hippocampi were dissected in ice-cold Hank's balanced salts solution (HBSS) and kept on ice until digestion with 0.2 µm-filtered 10 U/mL papain (Worthington Biochemical Corporation) in HBSS in a 37°C water bath for 20 min. Hippocampi were washed twice with HBSS and once with plating medium [MEM (Gibco) supplemented with 2 mM L-glutamine (Gibco), 0.4% glucose (Sigma), 2% Gem21 NeuroPlex Serum-Free Supplement (Gemini), and 5% fetal bovine serum (FBS, Atlanta)]. Cells were dissociated by trituration in plating media and plated onto glass coverslips coated with Matrigel Membrane Matrix (Corning) in 24-well plates (1 pup's hippocampi/12 wells). This day was considered day *in vitro* (DIV) 0. The next morning, on DIV1, 90% of the plating medium was replaced with fresh, pre-warmed growth medium (Neurobasal-A (Gibco) supplemented with 2% Gem21 NeuroPlex Serum-Free Supplement and 2 mM L-glutamine (Sigma)). At DIV3-4, when glia were ~70-80% confluent, 50% of the medium was replaced with fresh, pre-warmed plating medium and a final concentration of 2 µM cytosine arabinoside (AraC). At DIV8 and DIV12, 50% of the medium was replaced with fresh, pre-warmed plating medium. Analyses were performed at DIV14-16.

Pure Hippocampal Glia Cultures. Glial cultures were prepared using hippocampi pooled from male and female P1-P2 pups of wild-type CD-1 or *Nrxn1* HA-knockin mice. Tissue was digested with 0.2 µm-filtered 10 U/mL papain (Worthington Biochemical Corporation) in HBSS for 20 min at 37˚C, followed by harsh trituration to ensure low numbers of viable

neurons (McCarthy and De Vellis, 1980; Zhang et al., 2013). Dissociated hippocampal cells from 2 pups were pooled and plated in T25 flasks. Cells were plated in 90% Dulbecco's Modified Eagle Medium (DMEM) with 10% FBS and incubated at 37˚C and 5% CO_2. Medium was changed 24 h later and supplemented with 0.5% penicillin/streptomycin. Glial cultures were further purified once they reached 90% confluency 7 days later. Cells were rinsed three times, provided with fresh medium, and equilibrated for 2 h at 37˚C and 5% CO_2. To enrich astrocytes, flasks were transferred to an orbital shaker (250 RPM) for 15 h (McCarthy and De Vellis, 1980). After shaking, cells were rinsed three times and provided with fresh media. The cell layer following purification consisted of approximately 95% astrocytes. Re-plating of purified astrocytes was performed by detaching the cells with 0.05% trypsin for 5 min, centrifugation for 5 min at 1200 RPM, resuspending and plating at 30% confluence in 90% DMEM with 10% FBS (Zhang et al., 2013*)*. Astrocytes were replated on Matrigel-coated coverslips for immunofluorescence experiments or on 12-well culture plates for biochemical analysis. Cultured glia were analyzed once they achieved confluency around DIV14.

HEK293T cells. HEK293T cells (ATCC CRL-11268; female cell line) were grown in complete DMEM (cDMEM), which consisted of DMEM (Gibco), 5% FBS (Sigma), penicillin, and streptomycin. All transfections were performed using lipofectamine 3000 (Invitrogen). For co-culture assays, HEK293T cells were plated on 12-well plates and transfected at ~90% confluency according to manufacturer's instructions.

METHODS DETAILS

Tamoxifen Preparation and Injections. Tamoxifen (Sigma, Cat# T5648) stock was prepared by shaking 1 g of tamoxifen in 10 ml of 200-proof ethanol at room temperature (RT) for 15 min, followed by mixing with 90 ml of corn oil (Sigma, C8267) for 1-2 h at 37°C. Once fully dissolved, 1-ml aliquots (10 mg/ml tamoxifen) were stored at -20°C until use. Exposure to light was minimized at all times. For experiments using Aldh1l1-CreERT2 mice, mice were injected intraperitoneally on P10 and P11 with 80-90 µl tamoxifen stock using insulin syringes. To obtain both cKO and littermate controls and control for off-target effects of tamoxifen, entire litters were injected blind to genotype.

Plasmids. Lentiviruses expressing NLS-GFP-ΔCre or NLS-GFP-Cre driven by the human Synapsin promoter were described previously (Kaeser et al., 2011) and used for culture experiments (Fig. S3). For clustering assays, Nrxn1 ligands were cloned into mammalian expression vectors with tags that enabled detection of ligand expression on the cell surface (Fig. 4, S4). Human LRRTM2 was cloned into the pCMV5 vector and contained a PreProTrypsin signal peptide followed by an N-terminal flag sequence. Mouse neuroligin-1 cDNAs differing at splice site B (Boucard et al., 2005) were cloned into a lentiviral shuttle vector containing a ubiquitin promoter (i.e. FUW). An N-terminal flag sequence was placed after the native signal peptide. Mouse GluD1 was cloned into FUW by PCR amplification of

GluD1 cDNA (ORFeome Collaboration Clones, ID# 100068077) and an N-terminal flag sequence was placed after the native signal peptide. A novel membrane-tethered form of mouse neurexophilin-1 was generated by fusing mature neurexophilin-1 possessing an IgK signal peptide to the stalk region of mouse neurexin-3α in place of the LNS6 domain. A flexible linker sequence and flag sequence was inserted between mature neurexophilin-1 and the stalk region to facilitate proper protein folding. The chimeric fusion construct was cloned into FUW. Mouse cerebellin-1 was cloned into the episomal-type pEB-multi expression vector downstream of a CMV5 enhancer and Chicken actin (CAG) promotor sequence. A flag sequence was placed in the N-terminus after the signal peptide, and a tandem V5 and polyhistidine sequence was placed at the C-terminus. The Calsyntenin-3 plasmid was kindly provided by Dr. A. M. Craig (Pettem et al., 2013). The calsyntenin-3 construct contains an N-terminal myc sequence, a C-terminal mVenus sequence and deletion of a proteolytic cleavage site to enable better surface expression. Enhanced GFP (EGFP) was used to label transfected HEK293T cells. Empty backbone vectors (e.g. pcDNA3.0, pCMV5, and pEB multi) were used for co-transfection experiments.

Antibodies. The following antibodies were used at the indicated concentrations (IHC-immunohistochemistry; ICC-immunocytochemistry; IB-immunoblot): purified anti-HA mouse (Biolegend Cat# 901501; 1:500 live surface ICC, 1:500 ICC, 1:500 IHC, 1:1000 IB), anti-HA rabbit (Cell Signaling Cat#3724; 1:250 ICC), anti-Nrxn1 rabbit (Synaptic Systems Cat# 175103; 1:1000 IB), anti-pan-Nrxn rabbit (Frontier Institute Cat# Nrxn-Rb-Af870; 1:500 IB), anti-pan-Nrxn rabbit (homemade, G393; 1:500 IB), anti-pan-Nrxn rabbit (homemade, G394; 1:500 IB), anti-pan-Nrxn rabbit (Millipore Cat# ABN-161-I; 1:1000 IB), anti-GFAP mouse (Neuromab Cat# 75-240; 1:1000 IB, 1:1000 ICC, 1:500 IHC), anti-GFAP rabbit (Agilent Cat# Z0334; 1:1000 ICC, 1:1000 IHC), anti-GFAP chicken (Encorbio Cat# CPCA-GFAP; 1:1000 ICC, 1:1000 IHC), anti-heparan sulfate-stub 3G10 antibody mouse (Amsbio Cat# 370260-1; 1:1000 IB), anti-vGluT1 (Homemade YZ6089; 1:1000 IHC, 1:1000 IB), anti-MAP2 mouse (Sigma Cat# M1406; 1:1000 IHC), anti-NeuN mouse (Millipore Cat# MAB377; 1:1000 IHC), anti-NeuN rabbit (Cell Signaling Cat# 24307 1:1000 IHC), anti-ß-actin mouse (Sigma Cat#A1978; 1:3000 IB), anti-Synapsins rabbit (Homemade YZ6078; 1:500 ICC, 1:1000 IB), anti-Flag rat (Sigma Cat# SAB4200071; 1:500 surface ICC), anti-Myc rat (Abcam Cat# ab206486; 1:500 surface ICC), anti-VGAT guinea pig (Synaptic Systems Cat# 131005; 1:500 IHC), anti-GluN1 mouse (Synaptic Systems Cat# 114011; 1:1000 IB), anti-GluN2B mouse (Neuromab Cat# 75-101; 1:1000 IB), anti-GluR1 rabbit (Millipore Cat# Ab1504; 1:1000 IB), anti-GluR2 mouse (Neuromab Cat# 75-002; 1:1000 IB), anti-GluR4 (Millipore Cat# Ab1508; 1:1000 IB), anti-PSD-95 mouse (Neuromab Cat# 75-028; 1:1000 IB), anti-GRIP mouse (BD Transduction Cat# 611318, 1:1000 IB), anti-Gad67 mouse (Millipore Cat# mab5406; 1:1000 IB), anti-SNAP25 rabbit (Homemade P913; 1:500 IB), anti-Nlgn1 mouse (Synaptic Systems Cat# 129111; 1:1000 IB), anti-Nlgn2 rabbit (Synaptic Systems Cat# 129203; 1:1000 IB), anti-Nlgn3 mouse (Synaptic Systems Cat# 129311; 1:2000 IB), anti-GluD1 rabbit (Frontier Institute Cat# GluD1C-Rb-Af1390; 1:2000 IB), anti-CASK mouse (NeuroMab Cat# 75-000; 1:1000

IB). anti-Kir4.1 rabbit (Alomone Cat# APC-035; 1:2000 IB), anti-Glt1 guinea pig (Millipore Cat# AB1783; 1:1000 IB)

Cell and Tissue Lysis. Primary cultures (neurons and glia or glia only) plated in 24-well plates were isolated with 50–80 µl (per well) of ice-cold complete radioimmunoprecipitation assay (RIPA) lysis buffer containing 150 mM NaCl, 5 mM EDTA, 1% Triton X-100 (tx-100), 0.1% SDS, and 25 mM Tris-HCl, pH 7.6 in addition to 1X cOmplete ULTRA protease inhibitor cocktail (Roche, Cat# 11873580001). Fresh or snap-frozen hippocampal tissue was Dounce homogenized in 0.8-1.2 mL of cRIPA. Lysates were incubated on ice for 20 min and then clarified by centrifugation for 20 min at 13,000 rpm at 4°C. Cleared lysates were stored at −80°C until further processing.

Heparinase Treatment. Heparinase treatment of immunoprecipitated HA-Nrxn1 was performed as described previously (Zhang et al., 2018) but with some modifications. Each sample was subjected to two separate immunoprecipitation reactions allowing on-bead incubation of purified HA-Nrxn1 in reaction buffer with or without heparinases. Similar quantities of primary culture lysates (150 µg per reaction; Fig.3A) and brain tissue lysates (500 µg per reaction; Fig. 3G) were used. Lysates were rotated O/N with prewashed 1:1 anti-HA agarose beads (Sigma, Cat# A2095) at 4°C. Beads were then washed 1X with ice-cold wash buffer (100 mM NaCl, 20 mM Tris-HCl at pH 7, 1.5 mM $CaCl_2$, 1X protease inhibitors) containing 1% tx-100 and twice with wash buffer containing 0.2% tx-100. Beads were then incubated with 100 µl reaction buffer (containing: 1X NEB heparinase mix diluted in dH_2O, 1X cOmplete ULTRA protease inhibitor cocktail, and 0.2% tx-100) with or without 1 µl each of heparinases-I, -II, and -III (NEB) for 2 h at 30°C and 600 RPM. Beads were washed once with wash buffer containing 0.2% tx-100 to get rid of heparinases. Proteins were eluted with 60 ul of 2X Laemmli sample buffer with DTT at 65°C for 10 min.

Immunoblotting. Protein concentrations were determined with the BCA assay, using a BSA standard curve (Life Technologies Cat#23227). Samples were diluted in Laemmli sample buffer (final concentration: 1X) containing fresh DTT and heated to 95°C for 5 min. To limit protein aggregation caused by heating multi-pass transmembrane proteins (i.e. Glt-1, Kir4.1, and vGluT1), some samples were not heated. Proteins were separated by SDS-PAGE using 4–20% MIDI Criterion TGX precast gels (Bio-Rad). Generally, proteins were transferred onto 0.2 µm pore nitrocellulose membranes for 10 min at 2.5 V using the Trans-blot turbo transfer system (Bio-Rad). For more sensitive detection of neurexin levels, proteins were transferred onto nitrocellulose transfer membrane using a Criterion Blotter (Bio-Rad) with plate electrodes in ice-cold transfer buffer (25.1 mM Tris, 192 mM glycine, 20% methanol) at 80V constant voltage for 1 hr. Membranes were blocked in 5% non-fat milk (Carnation) diluted in PBS or TBS for 1 hr at RT. Membranes were then incubated with primary antibodies diluted in TBST (containing 0.1% Tween-20) overnight at 4°C. Beta-actin was used as a loading control for protein quantifications. Membranes were washed 3 times followed by incubation with secondary antibodies. Combinations of the following IRDye secondary antibodies were used (1:10,000 in TBST with 5% milk): IRDye

800CW donkey anti-mouse (926–32212), IRDye 680LT donkey anti-mouse (926–68022), IRDye 800CW donkey anti-rabbit (926–32213), IRDye 680LT donkey anti-rabbit (926–68023), and IRDye 680LT donkey anti-guinea pig (926-68030) from LI-COR. The Odyssey CLx imaging systems (LI-COR) was used to detect signal and was set to automatic mode for dynamic range detection. Pseudo-colors were applied to the signals, and quantification was performed using Image Studio 5.2. Normalization was performed as described in the figure legends.

Single-molecule in situ Hybridization and Immunocytochemistry. Wild-type CD-1 mice were euthanized with isoflurane at P30 followed by transcardial perfusion with ice-cold PBS. Brains were quickly dissected and embedded in Optimal Cutting Temperature (OCT) solution on dry ice. 12-µm thick sections were cut using a Leica cryostat (CM3050-S) and mounted directly onto Superfrost Plus histological slides and stored at −80°C until use. Combined single-molecule FISH and IHC for Nrxn1 mRNA (Advanced Cell Diagnostics, probe cat# 461511-C3) and mouse anti-GFAP antibody (Neuromab, Cat# 75-240) was performed using the multiplex RNAscope platform (Advanced Cell Diagnostics) according to manufacturer instructions for fresh-frozen sections. Briefly, after fixation and soon after *in situ* hybridization steps the slides were washed 2 times for 2 mins each with 1X TBST wash buffer. Slides were then incubated with 10% normal serum (TBS-1% BSA) for 30 mins at RT and proceeded with conventional IHC protocol. Primary and secondary Alexa antibodies were used at 1:500 dilution. Samples were mounted using Prolong Gold antifade mounting medium (ThermoFisher, Cat# P36930).

Purification of Ribosome-Bound mRNA. Ribosome-bound mRNA was purified as described previously (Sanz et al., 2009) but with modifications. Mice were euthanized using isoflurane and decapitated. Brains were quickly dissected and snap-frozen in liquid nitrogen and transferred to -80C storage until processing. Frozen brains were partially thawed in fresh homogenization buffer at 10% weight/volume and Dounce homogenized. For Baf53b-Cre/RiboTag mice, hippocampi from a single mouse represented a biological replicate, with 2 male and 2 female mice used in total. For Aldh1l1-CreERT2/RiboTag mice, hippocampi were pooled from 2 animals for a single biological replicate, and 4 replicates were made in total (2 sets of 2 male and 2 sets of 2 female mice). Homogenates were clarified by centrifugation and 10% of the supernatant was saved as input. The remaining lysate was incubated with pre-washed anti-HA magnetic beads (Thermo) overnight at 4°C. The beads were washed 3x with a high-salt buffer followed by elution with RLT lysis buffer containing 2-mercaptoethanol. Both input and IP samples were subjected to RNA extraction using the QIAGEN RNeasy Micro kit. RNA concentration was determined using a NanoDrop 1000 Spectrophotometer (Thermo) and stored at -80°C until downstream analysis.

Quantitative RT-PCR (qRT-PCR). For all quantitative RT-PCR experiments, RNA concentration was measured using a NanoDrop and equal quantities of RNA were used to synthesize cDNA with the SuperScript IV First Strand Synthesis Kit (Invitrogen, Cat#

18091050). Equal volumes of cDNA were then mixed with TaqMan Fast Virus 1-Step Master Mix (Thermo) and reactions were performed using the QuantStudio 3 RT-PCR System (Thermo). Transcripts were probed using PrimeTime qPCR Probe Assays (Integrated DNA Technologies), which consist of two primers and one FAM-labeled, ZEN/IBFQ-quenched 5' nuclease probe. Assays generating C_t values >35 were omitted. C_t values for technical replicates (duplicate or triplicate) differed by less than 0.5. C_t values were averaged for technical replicates. Data were normalized to the arithmetic mean of *ActB* or *Gapdh* using the $2^{-\Delta\Delta Ct}$ method.

For measuring the purity of cell type-specific ribosome-bound mRNA following immunoprecipitation (Fig. S2D), the following predesigned assays were used (gene, assay ID): Actb (Mm.PT.51.14022423), Aqp4 (Mm.PT.58.9080805), Sox9 (Mm.PT.58.42739087), PDGF (Mm.PT.56a.5639577), MBP (Mm.PT.58.28532164), P2ry12 (Mm.PT.58.43542033), and Rbfox3 or NeuN (Mm.PT.58.11398454).

To quantify the mRNA levels of Nrxn isoforms (Fig. 1B), the same mRNAs were probed using the following assays (gene, primer 1, primer 2, probe): Nrxn1αβγ (5'-CGATGTCATCTGTCCCAACA-3', 5'-GCCATCGGATTTAGCACTGTC-3', 5'-TGGAGCTGCACATACACCAAGGAA-3'), Nrxn1α (5'-TTCAAGTCCACAGATGCCAG-3', 5'-CAACACAAATCACTGCGGG-3', 5'- TGCCAAAAC/ZEN/TGGTCCATGCCAAAG-3'), Nrxn1β (5'-CCTGTCTGCTCGTGTACTG-3', 5'-TTGCAATCTACAGGTCACCAG-3', 5'-FAM/AGATATATG/ZEN/TTGTCCCAGCGTGTCCG-3'), Nrxn1γ (5'-GCCAGACAGACATGGATATGAG-3', 5'-GTCAATGTCCTCATCGTCACT-3', 5'-ACAGATGAC/ZEN/ATCCTTGTGGCCTCG-3'), Nrxn2α (5'-GTCAGCAACAACTTCATGGG-3', 5'-AGCCACATCCTCACAACG-3', 5'-FAM/CTTCATCTT/ZEN/CGGGTCCCCTTCCT-3'), Nrxn2β (5'-CCACCACTTCCACAGCAAG-3', 5'-CTGGTGTGTGCTGAAGCCTA-3', 5'-GGACCACAT/ZEN/ACAT CTTCGGG-3'), Nrxn3α (5'-GGGAGAACCTGCGAAAGAG-3', 5'-ATGAAGCGGAAGGACACATC-3', 5'- CTGCCGTCA/ZEN/TAGCTCAGGATAGATGC-3'), Nrxn3β (5'-CACCACTCTGTGCCTATTTC-3', 5'-GGCCAGGTATAGAGGATGA-3', 5'-TCTATCGCT/ZEN/CCCCTGTTTCC-3').

For qRT-PCR validation of RNAseq hits (Fig. 5), the following assays were used (gene name, assay ID): Syndig1 (Mm.PT.58.11714227), A2m (Mm.PT.58.8228034), C1ql3 (Mm.PT.58.27483950), Reln (Mm.PT.58.10165516), Nptx2 (Mm.PT.58.31290939), Ndnf (Mm.PT.56a.9101884), Ccl28 (Mm.PT.58.9726336), Gigyf1 (Mm.PT.58.5433296), Gnb2 (Mm.PT.58.5245057.g), Lrch4 (Mm.PT.58.41468474), Slc5a5 (Mm.PT.58.31918684), Hpgd (Mm.PT.56a.9684089), TMEM59l (Mm.PT.58.31528327.g), Vps37a (Mm.PT.58.9759868), Csgalnact1 (Mm.PT.58.32698019), GPR17 (Mm.PT.58.7204101), Mfap3l (Mm.PT.58.43969827), Hapln4 (Mm.PT.58.28564264), LPL (Mm.PT.58.46006099), Ocel1 (Mm.PT.58.5930413.g), and Plvap (Mm.PT.58.28447797). *Nrxn1* mRNA levels were evaluated using the above-mentioned primers, as well as a custom PCR assay recognizing the floxed *Nrxn1* exon. *Gapdh* (4352932E, Applied Biosystems) was used for

gene normalization. Validation was performed using the same RNA samples that were used for bulk RNAseq analysis with 4 biological replicates (2 males, 2 females) per genotype.

Junction-flanking qRT-PCR. Alternative splicing of *Nrxn1* mRNA was analyzed using junction-flanking PCR as published previously (Nguyen et al., 2016) but with modifications. The following primers anneal to constitutive exon sequences that flank splice junctions and thus amplify *Nrxn1* mRNA transcripts with or without alternative splice sequences (splice site, forward primer, reverse primer): SS1 (5'-GGCAAGGACTGCAGCCAA-3', 5'-ATCGCTGCTGCTTTGAATGG-3'), SS2 (5'-TGGGATCAGGGGCCTTTGAAGCA-3', 5'-GAAGGTCGGCTGTGCTGGGG-3'), SS3 (5'-GTGTGAAACTCACGGTCAATCTA-3', 5'-GTGCCATTCATTATCATTGAGGTTATAG-3'), SS4 (5'-CTGGCCAGTTATCGAACGCT-3', 5'-GCGATGTTGGCATCGTTCTC-3'), SS5 (5'-TTGACCCCTGTGAGCCGAGC-3', 5'-GGCTGCTGCGACAATCCCCA-3'), and SS6 (5'- AGGCTTTCAAGGTTGCCTGGCA-3', 5'-CCCATTGCTGCAAGCAAACGCC-3').

Splice-junction PCR was performed on cDNA synthesized from equal amounts of immunoprecipitated mRNA and total input RNA (Fig. 4). Splice-junction PCR was also performed on RNA purified from two-week old mixed hippocampal cultures (neurons and glia) and pure glia cultures (Fig. 4). Owing to relative differences in molecular weight of PCR products, running conditions were optimized to allow ideal resolution and band separation for quantification. Samples separated on 20% PAGE gels were stained using PAGE GelRed Nucleic Acid Gel Stain (Biotium). Homemade gels using standard agarose or MetaPhor Agarose were stained using GelRed. Stained gels were imaged at sub-saturation using the ChemiDoc Gel Imaging System (Bio-Rad). Quantification was performed using Image Lab (Bio-Rad) or ImageStudioLite (LI-COR). Intensity values were normalized to the size of DNA products to negate intensity differences related to increased dye incorporation with increased DNA length.

Synapse and Nrxn1 Clustering Assays. The heterologous synapse formation assay (Fig. 4I, 4J, S4C-S4F) was performed as described previously (Lee et al., 2017) but with modifications. HEK293T cells were plated in 12-well plates and transfected with Nrxn1 ligands and GFP plasmids using Lipofectamine 3000. At 16-24 h post-transfection, cells were lifted using DPBS containing 2 mM EDTA, spun down at 1200 RPM for 5 min and resuspended in neuronal growth media. In order to not overwhelm primary cultures, 100 µl of a 1:60-1:80 dilution of transfected HEK293T cells (per condition) was added per well of primary culture. Fresh cytosine arabinoside (AraC) was added to limit cell proliferation. The heterologous synapse formation assay was initiated by co-culturing mixed primary hippocampal cultures (neurons and glia) with HEK293T cells expressing Nrxn1 ligands or GFP for 48 hrs. At 48 hrs, cells were live-labeled for HA-Nrxn1 and fixed followed by staining for Nrxn1 ligands on the surface of HEK293T cells and synapse recruitment measured with antibodies raised against synapsins. For the astrocyte co-culture assay, mixed glia at 70-90% confluency (usually around DIV14) were co-cultured with HEK293T

cells for 48 h and then cells were live-labeled for surface HA-Nrxn1 and fixed. For testing the role of Nrxn1 heparin sulfate modification in synapse and HA-Nrxn1 recruitment, heparinases-I/II/III (NEB) were added at 0.4 units per ml beginning at 2 h prior to adding HEK293T cells and continuing throughout the 48 h co-culture period. Staining procedures are described in more detailed below.

Immunocytochemistry. For live surface-labeling experiments (Fig. 2, 4, S3, S4), primary cultures were washed once with ice-cold Dulbecco's PBS containing 1mM $MgCl_2$ and 1 mM $CaCl_2$ (PBS-MC). Cultures were then incubated on ice with mouse anti-HA (BioLegend) diluted 1:500 in PBS-MC for 30 min. Cultures were gently washed 3 times with cold PBS-MC and fixed for 20 min at RT with 4% (wt/vol) PFA. Following fixation, cultures were washed 2-3 times with DPBS. For surface-labeling experiments, cultures were blocked for 1 h at RT with antibody dilution buffer (ADB) without tx-100(-), which contains 5% normal goat serum diluted in DPBS. Cells were then labeled with Alexa Fluor-conjugated secondary antibodies (1:1000; Invitrogen) diluted in ADB(-) for 1 h at RT. For clustering assay experiments (Fig. 4, S4), cells were washed 3 times with DPBS and then briefly post-fixed for 10 min at RT with 4% PFA. They were then incubated with anti-Myc/Flag antibodies to label surface Nrxn1 ligands overnight at 4C followed by 3 washes, incubation with anti-Rat Alexa secondary antibodies, and 3 final washes.

For all immunocytochemistry experiments, cells were washed and then permeabilized and blocked for 1 h with ADB with tx-100(+) which contains 0.3% tx-100 and 5% normal goat serum diluted in DPBS. Non-surface primary antibodies were diluted in ADB(+) and cells were incubated in the cold-room overnight or for 2 h at RT (Fig. 2, 4, S3, S4). Cultures were washed three times with DPBS and then incubated with Alexa Fluor-conjugated secondary antibodies (1:1000; Invitrogen) diluted in ADB(+) for 1 h at RT. After three additional washes, coverslips were inverted onto glass microscope slides with Fluoromount-G mounting media (Southern Biotech).

Immunohistochemistry. Mice were anesthetized with isoflurane and then transcardially perfused (~1 ml/min) for 1 min with 0.1M DPBS (RT) followed by 7 min with 4% PFA (Electron Microscopy Services). For HA-Nrxn1 labeling (Fig. 2, S3), brains were post-fixed for 2 h at RT with 4% PFA. For all other stains brains were post-fixed in 4% PFA overnight at 4°C. Brains were washed 3 times with DPBS and cryoprotected by a 24-48 hr incubation in 30% sucrose w/v in DPBS. Brains were embedded in OCT Compound (Sakura), sectioned on the sagittal plane at 30-µm using a cryostat, and stored as floating sections in DPBS. For staining, free-floating sections were incubated with blocking buffer (containing 5% NGS and 0.3% tx-100 in DPBS) for 1 hr at RT. Sections were then incubated with primary antibodies diluted in blocking buffer overnight at 4°C on a rocker. After 3 washes, sections were incubated with Alexa dye secondary antibodies diluted in blocking buffer for 1-2 h at RT. Sections were washed 3-4 times and then mounted on charged glass slides. After drying, sections were dipped in water and allowed to dry again. Per slide, 4 droplets

of Fluormount-G with or without DAPI was added, slides were coverslipped, and nail polish was used to secure the coverslip until mounting medium hardened.

Generation of Sparse Nrxn1 cKO-T. Sparse deletion of Nrxn1 in astrocytes (Fig. 2C) was achieved via stereotactic injection of 1:5 diluted AAV5-GFAP-Cre-GFP (UNC Vector Core) into P2-P3 Nrxn1 HA-knockin pups with or without a single Ai14 tdTomato reporter allele. Mice were prepared for stereotactic injections using standard procedures approved by the Stanford University Administrative Panel on Laboratory Animal Care. Following anesthesia mice were injected unilaterally with 0.6-0.7 µl of virus using coordinates based on lambda (-1, 1, +/- -1.4 to -0.9). They were allowed to recover on a heating pad. Mice were perfused between P26-P30. Sections containing sparse fluorescent labeling (for Cre-GFP or tdTomato) were used for stained with mouse anti-HA (BioLegend) to recognize Nrxn1.

Confocal Microscopy. All confocal images were acquired at RT using an inverted Nikon A1RSi confocal microscope equipped with a 20x or 60x objective (Apo, NA 1.4) and operated by NIS-Elements AR acquisition software. In general, high magnification images were taken at 1,024 × 1,024 pixels with a z-stack distance of 0.3 µm. Low magnification images were taken at 1,024 x 1,024 pixels with Nyquist recommended step size. Line averaging (2X) was used for most images. Images were acquired sequentially in order to avoid bleed-through between channels. Imaging parameters (i.e., laser power, photomultiplier gain, offset, pinhole size, scan speed, etc.) were optimized to prevent pixel saturation and kept constant for all conditions within the same experiment. Images were analyzed using NIS-Elements Advanced Research software (Nikon). Post-imaging deconvolution was performed on images in Fig. 2C (right), which were acquired at Nyquist, to improve visualization of Nrxn1 puncta in the neuropil. For quantitative analysis, imaging of brain tissue involved imaging 2 regions of interest from at least 5 sections per animal. Quantitative analysis of vGAT-labeled inhibitory synapses (Fig. S6C) was performed using the General Analysis module in NIS-Elements to establish thresholds and determine object density, size, and intensity. For all other IHC stains, following background subtraction, intensities were averaged per animal in a given brain region or subregion and a minimum of 3 animals per genotype were analyzed. All IHC data was collected and analyzed blindly.

Transmission Electron Microscopy. Three pairs of P26 Nrxn1 astrocyte cKO mice and littermate controls (2 males and 1 female per genotype) were perfused with PBS followed by 4% paraformaldehyde w/v in PBS. The brains were dissected out and post-fixed in 2.5% glutaraldehyde and 2% paraformaldehyde in 0.1M sodium cacodylate buffer (pH 7.4) overnight at 4□C. The next day, 200- µm vibratome sections were collected in 0.1M cold cacodylate buffer and were re-fixed in 1% glutaraldehyde in 0.1M cacodylate buffer before being shipped to Yale CCMI EM facility. Hippocampal regions were dissected out and further post-fixed in 1% OsO_4, 0.8% potassium ferricyanide in 0.1 M cacodylate buffer at RT for 1 hour. Specimens were then *en bloc* stained with 2% aqueous uranyl acetate for 45 min, dehydrated in a graded series of ethanol to 100%, substituted with propylene oxide and embedded in EMbed 812 resin. Sample blocks were polymerized in an oven at 60°C

overnight. Thin sections (60 nm) were cut by a Leica ultramicrotome (UC7) and post-stained with 2% uranyl acetate and lead citrate. Sections were examined with a FEI Tecnai transmission electron microscope at 80 kV of accelerating voltage, digital images were recorded with an Olympus Morada CCD camera and iTEM imaging software. Approximately 30 electron micrographs were collected at random and analyzed for each animal in the stratum radiatum of CA1. Image analysis was performed using ImageJ while blind to genotype. Asymmetric excitatory synapses were identified based on the presence of a post-synaptic density and at least two presynaptic vesicles at the active zone. In addition, several morphological features of excitatory synapses were measured including postsynaptic area, PSD thickness, PSD length, number of synaptic vesicles per synaptic terminal, number of docked vesicles per synaptic junction, and width of the synaptic cleft. For statistical comparisons, density measurements were averaged per image and then averaged per animal. Synapse morphology measurements were only averaged per animal.

RNA Sequencing. Bulk hippocampal transcriptomic analysis was performed on Nrxn1 astrocyte and neuron cKO mice and littermate controls at P26-P30. To minimize batch effects and technical variability, 2 separate rounds of sequencing were performed on samples with 2 mice per genotype per round. In total, each genotype included 2 males and 2 females. Hippocampi were dissected and immediately mechanically homogenized in RLT Plus with 2-mercaptoethanol followed by centrifugation through a QIAshredder. RNA was extracted from the flow-through using the RNeasy Plus Mini Kit (QIAGEN). RNA was aliquoted into at least three tubes to minimize freeze-thaw cycles while allowing for QC analysis using a Bioanalyzer, RNA sequencing, and post-sequencing qPCR validation of differentially expressed genes. Library preparation, RNA and library quality measurements, and one-end sequencing were performed at a depth of 30 million reads by BGI in Hong Kong, China.

The R package DESeq2 was used to analyze differentially expressed genes using a negative binomial distribution, as described previously (Love et al., 2014). The DESeq data set was prepared based on the matrix of raw, un-normalized counts. The DESeq2 model internally corrected for library size, and the mean expected counts of each gene within each group were adjusted by normalization factors. As two separate rounds of sequencing were performed to account for batch variation, batch effects were controlled for in the design formula associated with the DESeq2 data set by using "batch" and “condition” variables to model the samples. Independent filtering of the mean normalized counts was performed using the “results” function, where a False Discovery Rate (FDR) threshold for adjusted p-values was set to alpha < 0.1. Genes of interest for subsequent qPCR validation were determined based on expression changes greater or less than 15% and p-values of less than 0.001, as well as adjusted p-values generally less than 0.05. Several genes with adjusted p-values between 0.2 and 0.05 were also tested. Volcano plots were generated using the VolcaNoseR package (https://huygens.science.uva.nl/VolcaNoseR/).

Electrophysiology. Acute transverse brain slices (300 μm) containing the dorsal hippocampus were prepared from P22-26 Nrxn1 brain, astrocyte, and neuron cKO mice and their WT littermates. Mice were anesthetized with isoflurane and decapitated. The brain was rapidly removed and placed into ice cold cutting solution containing the following (in mM): 205 sucrose, 2.5 KCl, 1.25 NaH_2PO_4, 25 $NaHCO_3$, 25 glucose, 0.4 ascorbic acid, 1 $CaCl_2$, 2 $MgCl_2$ and 3 sodium pyruvate in double-distilled water (ddH2O), pH 7.4 with NaOH, osmolality 300-305 mOsm saturated with 95% O2/5% CO2. Slices recovered at 31 °C in a 50:50 mixture composed of cutting saline and artificial cerebrospinal fluid (aCSF) containing the following (in mM): 123 NaCl, 2.5 KCl, 1.25 NaH_2PO_4, 25 $NaHCO_3$, 25 glucose, 2 $CaCl_2$ and 1 $MgCl_2$ in ddH2O and saturated with 95% O2/5% CO2, pH 7.4 with NaOH, osmolarity 300-305 mOsm for 30 min and then placed at RT in oxygenated aCSF alone for 1 hr. Whole-cell voltage clamp recordings were performed on CA1 pyramidal neurons. Brain slices were maintained at ~30°C via a dual-T344 temperature controller (Warner Instruments). Brain slices were continuously perfused with normal oxygenated aCSF (at about 1 ml/min perfusion rate) throughout recordings. Electrical signals were recorded at 25 kHz with a two channel Axoclamp 700B amplifier (Axon Instruments), digitalized with a Digidata 1440 digitizer (Molecular devices) that was in turn controlled by Clampex 10.7 (Molecular Devices). Recording pipettes were pulled from thin-walled borosilicate glass pipettes to resistances of 3-5 MΩ. mEPSCs and EPSCs were recorded with an internal solution containing (in mM): 117 Cs-methanesulfonate, 15 CsCl, 8 NaCl, 10 TEA-Cl, 0.2 EGTA, 4 Na_2-ATP, 0.3 Na_2-GTP, 10 HEPES, and 2 QX-314 pH pH 7.3 with CsOH (~300 mOsm). mEPSCs were recorded in 1 μM tetrodotoxin (TTX) and 100 μM picrotoxin. Miniature events were handpicked and analyzed in Clampfit 10 (Molecular Devices) using template matching and a threshold of 5 pA.

Evoked synaptic currents were elicited with a bipolar stimulating electrode (A-M Systems, Carlsborg, WA), controlled by a Model 2100 Isolated Pulse Stimulator (A-M Systems, Inc.), and synchronized with the Clampfit 10 data acquisition software (Molecular Devices). AMPA-receptor-mediated EPSCs were recorded at holding potentials of −70 mV, whereas NMDA-receptor-mediated EPSCs were recorded at +40 mV and quantified at 50 ms after the stimulus artifact. Measurements of the AMPAR/NMDAR ratio, AMPAR and NMDAR input-output curves were performed in 100 μM picrotoxin. Paired-pulse ratios were monitored with interstimulus intervals of 20-200 ms. LTP measurements in CA1 pyramidal neurons were performed using whole-cell patch-clamp recordings with the same extracellular and internal solutions, except the extracellular solution included picrotoxin (100 μM). Schaffer-collateral axons were stimulated extracellularly, and LTP was induced by two applications of 100 Hz stimuli separated by 10 s under voltage-clamp mode (holding potential = 0 mV). Pre-LTP (averaging last 5 mins as baseline) and post-LTP (averaging the last 5 mins) were recorded at 0.1 Hz. For all recordings and analyses, the experimenter was blind to genotype. Electrophysiological data were analyzed using Clampfit 10.4 (Molecular Devices).

Behavioral Analysis. Animals and housing**:** For behavioral phenotyping two cohorts of mice were tested. In total, n = 69 mice were used, including 36 female mice (including 20 Nrxn1 astrocyte cKO and 16 wild-type littermate controls) and 33 male mice (including 15 Nrxn1 astrocyte cKO and 18 wild-type littermate controls). In order to avoid litter effects, only litters with both genotypes were included in the experiments. Mice were identified by paw tattoo, using non-toxic animal tattoo ink (Ketchum permanent tattoo inks green paste, Ketchum Manufacturing Inc., Brockville, Canada). The ink was gently inserted subcutaneously through a 30-gauge hypodermic needle tip into the center of the paw during the first week of life. Then, mouse tail snips for genotyping were collected by dissecting ~0.3 cm of tail. All behavioral experiments were carried out between 7am and 7pm. All behavior assays were conducted and analyzed blind to genotype. Activity box, Y-maze, rotarod, nest building, and repetitive behavior was performed at the age of 2-4 months. Acoustic startle and pre-pulse inhibition of acoustic startle, and fear conditioning was performed at the age of 6-10 months.

Activity box: Locomotor activity, exploratory behavior and anxiety-related behavior were assessed under white light (circa 20 lux) in an activity box (ENV-510, 27.31 x 27.31 x 20.32 cm; Med Associates, Fairfax, VT, USA) using a modified protocol previously established (Rothwell et al., 2014). The activity box was housed within a sound-attenuating chamber, equipped with a ventilation fan and illuminated by a single overhead light. Mice were allowed to freely explore the activity box for 30 min. The position of the mouse within the arena was tracked in three dimensions by arrays of infrared light beams connected to a computer running Activity Monitor software (Med Associates, Fairfax, VT, USA). This software was used to calculate distance traveled, number of rearings, and time spent in the center during 1 min time bins, which were summed together to calculate total values throughout the entire 30 min test session. The center of the arena was defined as the center zone based on the central 75% in each dimension. Between each mouse, the activity box was thoroughly cleaned using 70% ethanol to avoid olfactory cues.

Y-maze: Spatial working memory in the Y-maze was measured under indirect red-light conditions using a modified protocol previously established (Zhou et al., 2018). A gray plastic Y-maze was used to evaluate spontaneous alternations reflecting spatial working memory. The maze consisted of three arms at 120° angles from each other (dimensions of each arm: 40□x□10□x□17□cm). Mice were individually placed in the distal end of one arm and allowed to freely explore the whole maze for 10□min. A completed arm entry was defined as the entering of the mouse with all four limbs. The sequence of arm entries was recorded and analyzed using the Viewer III tracking system (Biobserve, Bonn, Germany). Visiting all three different arms consecutively was termed a ‘correct’ triad and visiting one arm twice in three consecutive entries was termed a ‘wrong’ triad. Correct alternation percentage was calculated using the following formula: % Alternation = (Number of Alternations / [Total number of arm entries−2]) × 100. Between each mouse, the Y-maze was thoroughly cleaned using 70% ethanol to avoid olfactory cues.

Rotarod: Motor coordination and motor learning was tested under white light using a five-station rotarod treadmill (ENV-575M, Med Associates, Fairfax, VT, USA), as previously described (*54*). We performed the standard task with an accelerating rod from 4-40 rpm within 300 s. Testing consisted of 3 trials per day, separated by at least 60 min each, over the course of 2 days, i.e. 6 trials in total. On the first day of testing, mice were acclimated to the apparatus by being placed on the stationary rotarod for 30 s. The latency to falling off or making one complete revolution while hanging on was measured. A trial was stopped after 300 s (maximum speed, no further acceleration). Between each trial, the rotarod was thoroughly cleaned using 70% ethanol to avoid olfactory cues.

Nest building: Nest building was measured under white light using a modified protocol previously established (Etherton et al., 2009). After mice were habituated for 15 min to a novel cage with corn cob bedding but no other nest material, a 5 x 5 cm square of pressed cotton (Nestlet; Ancare, Bellmore, NY) was placed in a random cage corner, and nest width and nest height were measured after 90 min.

Repetitive behavior: Repetitive behavior was measured under white light (circa 40 lux) using a modified protocol previously established (Etherton et al., 2009). After mice were habituated for 10 min to a novel cage with corn cob bedding but no other nest material, self-grooming of all body regions was observed for 10 min by a trained observer using The Observer XT 11 software (Noldus, Wageningen, The Netherlands).

Acoustic startle response and pre-pulse inhibition of acoustic startle: Acoustic startle response and pre-pulse inhibition of acoustic startle were measured using the Kinder Scientific startle reflex system (Kinder Scientific, Poway, CA, USA), as previously described (Zhou et al., 2018). Data were analyzed with the Startle Monitor II software (Kinder Scientific). Mice were individually placed in a small cage atop a force plate within a sound attenuation chamber without light. Background noise was set at 65 dB. The startle response, defined as the change in amplitude of force in response to an unexpected acoustic stimulus, was measured. The peak values of the absolute force mice placed on the bottom of the cage were measured as the startle response. For the acoustic startle response experiment, 50 ms noise at 75, 85, 95, 105, and 115 dB were presented. Each stimulus was repeated 10 times. For the pre-pulse inhibition experiments, 50 ms noise at 115 dB was presented, with preceding noise at 0, 68, 71, or 77 dB. The acoustic startle response experiment had three phases. First, the startle response was determined by presenting 10 consecutive 115 dB pulse trials. The following trials were then presented 10 times each in pseudorandom order: 115 dB pulse with 0 dB pre-pulse, 68 dB pre-pulse, 71 dB pre-pulse, and 77 dB pre-pulse. The 115 dB pulse followed each pre-pulse at a 100 ms onset-onset interval. Then, the startle response was again determined by presenting 10 consecutive 115 dB pulse trials. The percent inhibition of the startle amplitude displayed during pulse trials was calculated for each pre-pulse/ pulse pair. For both experiments, mice were given 3 min of habituation time before the sound was delivered. Stimulus

sequence and inter-stimulus intervals were both pseudo-randomized. Between each trial, the cage was thoroughly cleaned using 70% ethanol to avoid olfactory cues.

Fear Conditioning. Fear conditioning was conducted using the Coulbourn fear conditioning system (Coulbourn Instruments, Holliston, MA, USA), as previously described (Zhou et al., 2018). Data were analyzed with the FreezeFrame software (ActiMetrics Software, Wilmette, IL, USA). On the training day, mice were individually placed in the fear conditioning chamber (18.5 x 18.5 x 21.5 cm; H10-11M-TC; Coulbourn Instruments) outfitted with a metal grid floor and located in the center of a sound attenuating cubicle with white house light (Coulbourn Instruments). The conditioning chamber was cleaned with 70% ethanol to set background odor level. A ventilation fan provided background noise at ~55 dB. As the conditioned stimulus (CS), a 2 kHz tone was presented at 85 dB for 30 s. As the unconditioned stimulus (US), a 0.75 mA foot shock was applied for 2 s through the Coulbourn precision animal shocker (Coulbourn Instruments). The foot shock co-terminated with the tone. After a 2 min habituation period, 3 CS-US pairings separated by 1 min inter-stimulus intervals (ISI) were delivered. Mice remained in the conditioning chamber for another 60 s before being returned to their home cages. Between each mouse, the conditioning chamber was thoroughly cleaned using 70% ethanol to avoid olfactory cues. In the context test, 24 h after training, mice were placed back into the original conditioning chamber for 5 min to assess contextual recall. During the altered context test, 48 h after training, the conditioning chamber was modified by changing its metal grid floor to a plastic sheet, white metal side walls to plastic walls decorated with stripes of various colors, and the background odor of 70% ethanol to 1% vanilla. Mice were placed in the altered chamber for 5 min. After this 5 min period, the CS was delivered for 1 min to assess cued recall. Finally, 2 months later, mice were again exposed to the original conditioning chamber for 5 min to assess remote contextual recall. Freezing behavior defined as a bout of motionless lasting 1 s or longer was recorded and analyzed automatically in 30 s time bins using the FreezeFrame software.

Fur Lesions. Fur lesions were scored immediately before measuring remote contextual recall at ~12 months.

QUANTIFICATION AND STATISTICAL ANALYSIS

Quantifications have been described in the respective materials and methods sections, and statistical details are provided in the figure legends. Statistical significance between various conditions was assessed by determining p-values (95% confidence interval). For animal survival analysis and quantitative immunoblotting experiments, statistical analyses were performed using GraphPad Prism 6 software. Blot intensity quantification was performed using Image Studio Lite. For most staining experiments, the “n” represents the average per animal or average per culture. In contrast, for electrophysiology measurements, the “n” represents the total number of cells patched. For biochemical and

behavioral experiments, the “n” generally represents number of animals, independent cultures or pooled samples. Most intergroup comparisons were done by two-tailed Student’s t test or the Mann Whitney Test. For multiple comparisons, data were analyzed with one- or two-way ANOVA followed by a post-hoc test (e.g. Tukey’s). Levels of significance were set as * $p < 0.05$; ** $p < 0.01$; *** $p < 0.001$; **** $p < 0.0001$. All graphs depict means ± SEM.

DATA AND CODE AVAILABILITY

No code is generated in this study. The data that support the findings of this study are available from the Lead Contact upon request.

LEAD CONTACT AND MATERIALS AVAILABILITY

Further information and requests for resources and reagents should be directed to and will be fulfilled by the lead contact, Thomas C. Südhof (tcs1@stanford.edu). All unique/stable reagents generated in this study are available from the Lead Contact without restriction.

ACKNOWLEDGEMENTS

We would like to thank Ben Barres, Shane Liddelow and other members of the Barres lab family for discussions, reagents and technical assistance. We thank Ann Marie Craig for the Calsyntenin-3 construct and Anna Kalaj for helping review the manuscript and insightful discussions. This study was supported by grants from NIMH (MH052804 and MH104172 to T.C.S.; by F32-MH105040 to J.H.T.). M.W. was supported by a Feodor Lynen fellowship for experienced researchers from the Alexander von Humboldt Foundation.

AUTHOR CONTRIBUTIONS

J.T. performed the genetic, biochemical, and imaging experiments, Z.D. the electrophysiology experiments, K.R. contributed to Ribotag experiments, S.E.P. contributed to culture experiments, A.N. contributed to RNAseq experiments, X.L. performed the electron microscopy, M.W. performed the behavioral experiments, and K.L. performed the *in situ* hybridizations and contributed to the splicing experiments. J.T. and

T.C.S. conceived and planned the project, analyzed the data, and wrote the paper with input from all authors.

COMPETING INTERESTS

Authors declare no competing interests.

REFERENCES

Allen, N.J., Bennett, M.L., Foo, L.C., Wang, G.X., Chakraborty, C., Smith, S.J., and Barres, B.A. (2012). Astrocyte glypicans 4 and 6 promote formation of excitatory synapses via GluA1 AMPA receptors. Nature *486*, 410–414.

Anderson, G.R., Aoto, J., Tabuchi, K., Foldy, C., Covy, J., Yee, A.X., Wu, D., Lee, S.J., Chen, L., Malenka, R.C., et al. (2015). beta-Neurexins Control Neural Circuits by Regulating Synaptic Endocannabinoid Signaling. Cell *162*, 593–606.

Aoto, J., Martinelli, D.C., Malenka, R.C., Tabuchi, K., and Südhof, T.C. (2013). Presynaptic neurexin-3 alternative splicing trans-synaptically controls postsynaptic AMPA receptor trafficking. Cell *154*, 75–88.

Bekku, Y., Su, W.D., Hirakawa, S., Fässler, R., Ohtsuka, A., Kang, J.S., Sanders, J., Murakami, T., Ninomiya, Y., and Oohashi, T. (2003). Molecular cloning of Bral2, a novel brain-specific link protein, and immunohistochemical colocalization with brevican in perineuronal nets. Mol. Cell. Neurosci. *24*, 148–159.

Bhouri, M., Morishita, W., Temkin, P., Goswami, D., Kawabe, H., Brose, N., Südhof, T.C., Craig, A.M., Siddiqui, T.J., and Malenka, R. (2018). Deletion of LRRTM1 and LRRTM2 in adult mice impairs basal AMPA receptor transmission and LTP in hippocampal CA1 pyramidal neurons. Proc. Natl. Acad. Sci. U. S. A. *115*, E5382–E5389

Blanco-Suarez, E., Liu, T.F., Kopelevich, A., and Allen, N.J. (2018). Astrocyte-Secreted Chordin-like 1 Drives Synapse Maturation and Limits Plasticity by Increasing Synaptic GluA2 AMPA Receptors. Neuron *100*, 1116–1132.

Bohmbach, K., Schwarz, M.K., Schoch, S., and Henneberger, C. (2018). The structural and functional evidence for vesicular release from astrocytes in situ. Brain Res. Bull. *136*, 65–75.

Boucard, A.A., Chubykin, A.A., Comoletti, D., Taylor, P., and Südhof, T.C. (2005). A splice code for trans-synaptic cell adhesion mediated by binding of neuroligin 1 to α- and β-neurexins. Neuron *48*, 229–236.

Chen, L.Y., Jiang, M., Zhang, B., Gokce, O., and Sudhof, T.C. (2017). Conditional Deletion of All Neurexins Defines Diversity of Essential Synaptic Organizer Functions for Neurexins. Neuron *94*, 611-625.

Chih, B., Gollan, L., and Scheiffele, P. (2006). Alternative Splicing Controls Selective Trans-Synaptic Interactions of the Neuroligin-Neurexin Complex. Neuron. *51*, 171-178.

Christopherson, K.S., Ullian, E.M., Stokes, C.C.A., Mullowney, C.E., Hell, J.W., Agah, A., Lawler, J., Mosher, D.F., Bornstein, P., and Barres, B.A. (2005). Thrombospondins are astrocyte-secreted proteins that promote CNS synaptogenesis. Cell *120*, 421–433.

Comoletti, D., Flynn, R.E., Boucard, A.A., Demeler, B., Schirf, V., Shi, J., Jennings, L.L., Newlin, H.R., Südhof, T.C., and Taylor, P. (2006). Gene selection, alternative splicing, and post-translational processing regulate neuroligin selectivity for β-neurexins. Biochemistry *45*, 12816-12827.

Dai, J., Aoto, J., and Südhof, T.C. (2019). Alternative Splicing of Presynaptic Neurexins Differentially Controls Postsynaptic NMDA and AMPA Receptor Responses. Neuron *102*, 993–1008

David, G., Bai, X.M., Van Der Schueren, B., Cassiman, J.J., and Van Den Berghe, H. (1992). Developmental changes in heparan sulfate expression: In situ detection with mAbs. J. Cell Biol. *119*, 961–975.

Dietz, A.G., Goldman, S.A., and Nedergaard, M. (2020). Glial cells in schizophrenia: a unified hypothesis. The Lancet Psychiatry *7*, 272–281.

DiLalla, L.F., McCrary, M., and Diaz, E. (2017). A review of endophenotypes in schizophrenia and autism: The next phase for understanding genetic etiologies. Am. J. Med. Genet. Part C Semin. Med. Genet. *175*, 354–361.

Diniz, L.P., Almeida, J.C., Tortelli, V., Lopes, C.V., Setti-Perdigão, P., Stipursky, J., Kahn, S.A., Romão, L.F., De Miranda, J., Alves-Leon, S.V., et al. (2012). Astrocyte-induced synaptogenesis is mediated by transforming growth factor β signaling through modulation of d-serine levels in cerebral cortex neurons. J. Biol. Chem. *287*, 41432–41445.

Durkee, C.A., and Araque, A. (2019). Diversity and Specificity of Astrocyte–neuron Communication. Neuroscience *396*, 73–78.

Elegheert, J., Cvetkovska, V., Clayton, A.J., Heroven, C., Vennekens, K.M., Smukowski, S.N., Regan, M.C., Jia, W., Smith, A.C., Furukawa, H., et al. (2017). Structural Mechanism for Modulation of Synaptic Neuroligin-Neurexin Signaling by MDGA Proteins. Neuron. *95*, 896-913.

Etherton, M.R., Blaiss, C.A., Powell, C.M., and Südhof, T.C. (2009). Mouse neurexin-1α deletion causes correlated electrophysiological and behavioral changes consistent with cognitive impairments. Proc. Natl. Acad. Sci. U. S. A. *106*, 17998–18003.

Farhy-Tselnicker, I., and Allen, N.J. (2018). Astrocytes, neurons, synapses: A tripartite view on cortical circuit development. Neural Dev. *13*.

Fuccillo, M. V., Földy, C., Gökce, Ö., Rothwell, P.E., Sun, G.L., Malenka, R.C., and Südhof, T.C. (2015). Single-Cell mRNA Profiling Reveals Cell-Type-Specific Expression of Neurexin Isoforms. Neuron *87*, 326–340.

Graf, E.R., Zhang, X., Jin, S.-X., Linhoff, M.W., and Craig, A.M. (2004). Neurexins induce differentiation of GABA and glutamate postsynaptic specializations via neuroligins. Cell *119*, 1013–1026.

Hodge, R.D., Bakken, T.E., Miller, J.A., Smith, K.A., Barkan, E.R., Graybuck, L.T., Close, J.L., Long, B., Johansen, N., Penn, O., et al. (2019). Conserved cell types with divergent features in human versus mouse cortex. Nature *573*, 61–68.

Hu, Z., Xiao, X., Zhang, Z., and Li, M. (2019). Genetic insights and neurobiological implications from NRXN1 in neuropsychiatric disorders. Mol. Psychiatry *24*, 1400–1414.

Ichtchenko, K., Hata, Y., Nguyen, T., Ullrich, B., Missler, M., Moomaw, C., and Südhof, T.C. (1995). Neuroligin 1: A splice site-specific ligand for β-neurexins. Cell *81*, 435–443.

Ichtchenko, K., Nguyen, T., and Südhof, T.C. (1996). Structures, alternative splicing, and neurexin binding of multiple neuroligins. J. Biol. Chem. *271*, 2676–2682.

Javitt, D.C., and Freedman, R. (2015). Sensory processing dysfunction in the personal experience and neuronal machinery of schizophrenia. Am. J. Psychiatry *172*, 17–31.

Joo, J.Y., Lee, S.J., Uemura, T., Yoshida, T., Yasumura, M., Watanabe, M., and Mishina, M. (2011). Differential interactions of cerebellin precursor protein (Cbln) subtypes and neurexin variants for synapse formation of cortical neurons. Biochem. Biophys. Res. Commun. *406*, 627–632.

Kaeser, P.S., Deng, L., Wang, Y., Dulubova, I., Liu, X., Rizo, J., and Südhof, T.C. (2011). RIM proteins tether Ca2+channels to presynaptic active zones via a direct PDZ-domain interaction. Cell *144*, 282–295.

Kalashnikova, E., Lorca, R.A., Kaur, I., Barisone, G.A., Li, B., Ishimaru, T., Trimmer, J.S., Mohapatra, D.P., and Díaz, E. (2010). SynDIG1: An Activity-Regulated, AMPA- Receptor-Interacting Transmembrane Protein that Regulates Excitatory Synapse Development. Neuron *65*, 80–93.

Kasem, E., Kurihara, T., and Tabuchi, K. (2018). Neurexins and neuropsychiatric disorders. Neurosci. Res. *127*, 53–60.

Khalaj, A.J., Sterky, F.H., Sclip, A., Schwenk, J., Brunger, A.T., Fakler, B., and Südhof, T.C. (2020). Deorphanizing FAM19A proteins as pan-neurexin ligands with an unusual biosynthetic binding mechanism. J. Cell Biol. *219*, e202004164.

Kikuchi, T., Gonzalez-Soriano, J., Kastanauskaite, A., Benavides-Piccione, R., Merchan-Perez, A., DeFelipe, J., and Blazquez-Llorca, L. (2020). Volume Electron Microscopy Study of the Relationship Between Synapses and Astrocytes in the Developing Rat Somatosensory Cortex. Cereb. Cortex. *30*, 3800–3819.

Ko, J., Fuccillo, M. V, Malenka, R.C., and Südhof, T.C. (2009). LRRTM2 functions as a neurexin ligand in promoting excitatory synapse formation. Neuron *64*, 791–798.

Koeppen, J., Nguyen, A.Q., Nikolakopoulou, A.M., Garcia, M., Hanna, S., Woodruff, S., Figueroa, Z., Obenaus, A., and Ethell, I.M. (2018). Functional consequences of synapse remodeling following astrocyte-specific regulation of ephrin-B1 in the adult hippocampus. J. Neurosci. *38*, 5710–5726.

Kucukdereli, H., Allen, N.J., Lee, A.T., Feng, A., Ozlu, M.I., Conatser, L.M., Chakraborty, C., Workman, G., Weaver, M., Sage, E.H., et al. (2011). Control of excitatory CNS synaptogenesis by astrocyte-secreted proteins hevin and SPARC. Proc. Natl. Acad. Sci. U. S. A. *108*, E440–449.

Kwon, H.B., Kozorovitskiy, Y., Oh, W.J., Peixoto, R.T., Akhtar, N., Saulnier, J.L., Gu, C., and Sabatini, B.L. (2012). Neuroligin-1-dependent competition regulates cortical synaptogenesis and synapse number. Nat. Neurosci. *15*, 1667–1674.

Lee, S.J., Wei, M., Zhang, C., Maxeiner, S., Pak, C.H., Botelho, S.C., Trotter, J., Sterky, F.H., and Südhof, T.C. (2017). Presynaptic neuronal pentraxin receptor organizes excitatory and inhibitory synapses. J. Neurosci. *37*, 1062–1080.

Liu, J., Shelkar, G.P., Gandhi, P.J., Gawande, D.Y., Hoover, A., Villalba, R.M., Pavuluri, R., Smith, Y., and Dravid, S.M. (2020). Striatal glutamate delta-1 receptor regulates behavioral flexibility and thalamostriatal connectivity. Neurobiol. Dis. *137*, 104746.

Love, M.I., Huber, W., and Anders, S. (2014). Moderated estimation of fold change and dispersion for RNA-seq data with DESeq2. Genome Biol. *15*, 550.

Lukacsovich, D., Winterer, J., Que, L., Luo, W., Lukacsovich, T., and Földy, C. (2019). Single-Cell RNA-Seq Reveals Developmental Origins and Ontogenetic Stability of Neurexin Alternative Splicing Profiles. Cell Rep. *27*, 3752–3759.

Luo, F., Sclip, A., Jiang, M., and Südhof, T.C. (2020). Neurexins cluster Ca 2+ channels within the presynaptic active zone. EMBO J. *39*, e103208.

Marshall, C.R., Howrigan, D.P., Merico, D., Thiruvahindrapuram, B., Wu, W., Greer, D.S., Antaki, D., Shetty, A., Holmans, P.A., Pinto, D., et al. (2017). Contribution of copy number variants to schizophrenia from a genome-wide study of 41,321 subjects. Nat. Genet. *49*, 27-35.

Matsuda, K., Budisantoso, T., Mitakidis, N., Sugaya, Y., Miura, E., Kakegawa, W., Yamasaki, M., Konno, K., Uchigashima, M., Abe, M., et al. (2016). Transsynaptic Modulation of Kainate Receptor Functions by C1q-like Proteins. Neuron *90*, 752–767.

Matsuda, K. and Yuzaki, M. (2011). Cbln family proteins promote synapse formation by regulating distinct neurexin signaling pathways in various brain regions. Eur J Neurosci. *33*, 1447–1461.

McCarthy, K.D., and De Vellis, J. (1980). Preparation of separate astroglial and oligodendroglial cell cultures from rat cerebral tissue. J. Cell Biol. *85*, 890–902.

Missler, M., Zhang, W., Rohlmann, A., Kattenstroth, G., Hammer, R.E., Gottmann, K., and Südhof, T.C. (2003). α-neurexins couple Ca 2+ channels to synaptic vesicle exocytosis. Nature *423*, 939–948.

Nagai, J., Rajbhandari, A.K., Gangwani, M.R., Hachisuka, A., Coppola, G., Masmanidis, S.C., Fanselow, M.S., and Khakh, B.S. (2019). Hyperactivity with Disrupted Attention by Activation of an Astrocyte Synaptogenic Cue. Cell *177*, 1280–1292.

Nam, C.I. and Chen, L. (2005). Postsynaptic assembly induced by neurexin-neuroligin interaction and neurotransmitter. Proc. Natl. Acad. Sci. U. S. A. *102*, 6137-6142.

Nguyen, T.M., Schreiner, D., Xiao, L., Traunmüller, L., Bornmann, C., and Scheiffele, P. (2016). An alternative splicing switch shapes neurexin repertoires in principal neurons versus interneurons in the mouse hippocampus. Elife *5*, e22757.

O'Brien, R.J., Desheng, X., Petralia, R.S., Steward, O., Huganir, R.L., and Worley, P. (1999). Synaptic clustering of AMPA receptors by the extracellular immediate- early gene product Narp. Neuron *23*, 309–323.

Papouin, T., Dunphy, J., Tolman, M., Foley, J.C., and Haydon, P.G. (2017). Astrocytic control of synaptic function. Philos. Trans. R. Soc. B Biol. Sci. *372*.

Perez, J.M., Berto, S., Gleason, K., Ghose, S., Tan, C., Kim, T.K., Konopka, G., and Tamminga, C.A. (2020). Hippocampal subfield transcriptome analysis in schizophrenia psychosis. Mol. Psychiatry. doi: 10.1038/s41380-020-0696-6.

Pettem, K.L., Yokomaku, D., Luo, L., Linhoff, M.W., Prasad, T., Connor, S.A., Siddiqui, T.J., Kawabe, H., Chen, F., Zhang, L., et al. (2013). The Specific α-Neurexin Interactor Calsyntenin-3 Promotes Excitatory and Inhibitory Synapse Development. Neuron *80*, 113–128.

Poulopoulos, A., Aramuni, G., Meyer, G., Soykan, T., Hoon, M., Papadopoulos, T., Zhang, M., Paarmann, I., Fuchs, C., Harvey, K., et al. (2009). Neuroligin 2 Drives Postsynaptic Assembly at Perisomatic Inhibitory Synapses through Gephyrin and Collybistin. Neuron. *63*, 628-642.

Rees, E., Walters, J.T.R., Georgieva, L., Isles, A.R., Chambert, K.D., Richards, A.L., Mahoney-Davies, G., Legge, S.E., Moran, J.L., McCarroll, S.A., et al. (2014). Analysis of copy number variations at 15 schizophrenia-associated loci. Br. J. Psychiatry *204*, 108–114.

Roppongi, R.T., Karimi, B., and Siddiqui, T.J. (2017). Role of LRRTMs in synapse development and plasticity. Neurosci. Res. *116*, 18-28.

Roppongi, R.T., Dhume, S.H., Padmanabhan, N., Silwal, P., Zahra, N., Karimi, B., Bomkamp, C., Patil, C.S., Champagne-Jorgensen, K., Twilley, R.E., et al. (2020). LRRTMs Organize Synapses through Differential Engagement of Neurexin and PTPσ. Neuron *106*, 108–125.

Rothwell, P.E., Fuccillo, M. V., Maxeiner, S., Hayton, S.J., Gokce, O., Lim, B.K., Fowler, S.C., Malenka, R.C., and Südhof, T.C. (2014). Autism-associated neuroligin-3 mutations commonly impair striatal circuits to boost repetitive behaviors. Cell *158*, 198–212.

Sanz, E., Yang, L., Su, T., Morris, D.R., McKnight, G.S., and Amieux, P.S. (2009). Cell-type-specific isolation of ribosome-associated mRNA from complex tissues. Proc. Natl. Acad. Sci. U. S. A. *106*, 13939–13944.

Saunders, A., Macosko, E.Z., Wysoker, A., Goldman, M., Krienen, F.M., de Rivera, H., Bien, E., Baum, M., Bortolin, L., Wang, S., et al. (2018). Molecular Diversity and Specializations among the Cells of the Adult Mouse Brain. Cell *174*, 1015-1030.

Schaum, N., Karkanias, J., Neff, N.F., May, A.P., Quake, S.R., Wyss-Coray, T., Darmanis, S., Batson, J., Botvinnik, O., Chen, M.B., et al. (2018). Single-cell transcriptomics of 20 mouse organs creates a Tabula Muris. Nature *562*, 367–372.

Scheiffele, P., Fan, J., Choih, J., Fetter, R., and Serafini, T. (2000). Neuroligin expressed in nonneuronal cells triggers presynaptic development in contacting axons. Cell 101, 657-669.

Schreiner, D., Nguyen, T.M., Russo, G., Heber, S., Patrignani, A., Ahrne, E., and Scheiffele, P. (2014). Targeted combinatorial alternative splicing generates brain region-specific repertoires of neurexins. Neuron *84*, 386–398.

Siddiqui, T.J., Pancaroglu, R., Kang, Y., Rooyakkers, A., and Craig, A.M. (2010). LRRTMs and neuroligins bind neurexins with a differential code to cooperate in glutamate synapse development. J. Neurosci. *30*, 7495–7506.

Srinivasan, R., Lu, T.Y., Chai, H., Xu, J., Huang, B.S., Golshani, P., Coppola, G., and Khakh, B.S. (2016). New Transgenic Mouse Lines for Selectively Targeting Astrocytes and Studying Calcium Signals in Astrocyte Processes In Situ and In Vivo. Neuron *92*, 1181–1195.

Sterky, F.H., Trotter, J.H., Lee, S.J., Recktenwald, C. V, Du, X., Zhou, B., Zhou, P., Schwenk, J., Fakler, B., and Sudhof, T.C. (2017). Carbonic anhydrase-related protein CA10 is an evolutionarily conserved pan-neurexin ligand. Proc Natl Acad Sci U S A *114*, E1253–E1262.

Stogsdill, J.A., Ramirez, J., Liu, D., Kim, Y.H., Baldwin, K.T., Enustun, E., Ejikeme, T., Ji, R.R., and Eroglu, C. (2017). Astrocytic neuroligins control astrocyte morphogenesis and synaptogenesis. Nature *551*, 192-197.

Sudhof, T.C. (2017). Synaptic Neurexin Complexes: A Molecular Code for the Logic of Neural Circuits. Cell *171*, 745–769.

Südhof, T.C. (2018). Towards an Understanding of Synapse Formation. Neuron. *100*, 276-293.

Tasic, B., Yao, Z., Graybuck, L.T., Smith, K.A., Nguyen, T.N., Bertagnolli, D., Goldy, J., Garren, E., Economo, M.N., Viswanathan, S., et al. (2018). Shared and distinct transcriptomic cell types across neocortical areas. Nature *563*, 72–78.

Treutlein, B., Gokce, O., Quake, S.R., and Sudhof, T.C. (2014). Cartography of neurexin alternative splicing mapped by single-molecule long-read mRNA sequencing. Proc Natl Acad Sci U S A *111*, E1291–9.

Trotter, J.H., Hao, J., Maxeiner, S., Tsetsenis, T., Liu, Z., Zhuang, X., and Südhof, T.C. (2019). Synaptic neurexin-1 assembles into dynamically regulated active zone nanoclusters. J. Cell Biol. *218*, 2677-2698.

Uemura, T., Lee, S.-J., Yasumura, M., Takeuchi, T., Yoshida, T., Ra, M., Taguchi, R., Sakimura, K., and Mishina, M. (2010). Trans-synaptic interaction of GluRdelta2 and Neurexin through Cbln1 mediates synapse formation in the cerebellum. Cell *141*, 1068–1079.

Ullrich, B., Ushkaryov, Y.A., and Südhof, T.C. (1995). Cartography of neurexins: more than 1000 isoforms generated by alternative splicing and expressed in distinct subsets of neurons. Neuron *14*, 497–507.

Ushkaryov, Y.A., and Sudhof, T.C. (1993). Neurexin III alpha: extensive alternative splicing generates membrane-bound and soluble forms. Proc Natl Acad Sci U S A *90*, 6410–6414.

Ushkaryov, Y.A., Petrenko, A.G., Geppert, M., and Südhof, T.C. (1992). Neurexins: Synaptic cell surface proteins related to the α-latrotoxin receptor and laminin. Science *257*, 50–56.

Ushkaryov, Y.A., Hata, Y., Ichtchenko, K., Moomaw, C., Afendis, S., Slaughter, C.A., and Südhof, T.C. (1994). Conserved domain structure of beta-neurexins. Unusual cleaved signal sequences in receptor-like neuronal cell-surface proteins. J. Biol. Chem. *269*, 11987–11992.

Varoqueaux, F., Aramuni, G., Rawson, R.L., Mohrmann, R., Missler, M., Gottmann, K., Zhang, W., Südhof, T.C., and Brose, N. (2006). Neuroligins Determine Synapse Maturation and Function. Neuron *51*, 741–754.

Ventura, R., and Harris, K.M. (1999). Three-dimensional relationships between hippocampal synapses and astrocytes. J. Neurosci *58*, 572–587.

Yan, Q., Weyn-Vanhentenryck, S.M., Wu, J., Sloan, S.A., Zhang, Y., Chen, K., Wu, J.Q., Barres, B.A., and Zhang, C. (2015). Systematic discovery of regulated and conserved alternative exons in the mammalian brain reveals NMD modulating chromatin regulators. Proc Natl Acad Sci U S A *112*, 3445–3450.

Yu, X., Nagai, J., and Khakh, B.S. (2020). Improved tools to study astrocytes. Nat. Rev.

Neurosci. *21*, 121-138.

Yuzaki, M. (2018). Two Classes of Secreted Synaptic Organizers in the Central Nervous System. Annu. Rev. Physiol. *80*, 243–262.

Zeisel, A., Hochgerner, H., Lönnerberg, P., Johnsson, A., Memic, F., van der Zwan, J., Häring, M., Braun, E., Borm, L.E., La Manno, G., et al. (2018). Molecular Architecture of the Mouse Nervous System. Cell *174*, 999–1014.

Zhan, X., Cao, M., Yoo, A.S., Zhang, Z., Chen, L., Crabtree, G.R., and Wu, J.I. (2015). Generation of BAF53b-Cre transgenic mice with pan-neuronal Cre activities. Genesis *53*, 440–448.

Zhang, P., Lu, H., Peixoto, R.T., Pines, M.K., Ge, Y., Oku, S., Siddiqui, T.J., Xie, Y., Wu, W., Archer-Hartmann, S., et al. (2018). Heparan Sulfate Organizes Neuronal Synapses through Neurexin Partnerships. Cell *174*, 1450–1464.

Zhang, Y., Pak, C.H., Han, Y., Ahlenius, H., Zhang, Z., Chanda, S., Marro, S., Patzke, C., Acuna, C., Covy, J., et al. (2013). Rapid single-step induction of functional neurons from human pluripotent stem cells. Neuron *78*, 785–798.

Zhou, M., Liu, Z., Melin, M.D., Ng, Y.H., Xu, W., and Südhof, T.C. (2018). A central amygdala to zona incerta projection is required for acquisition and remote recall of conditioned fear memory. Nat. Neurosci. *21*, 1515–1519.

FIGURES and FIGURE LEGENDS

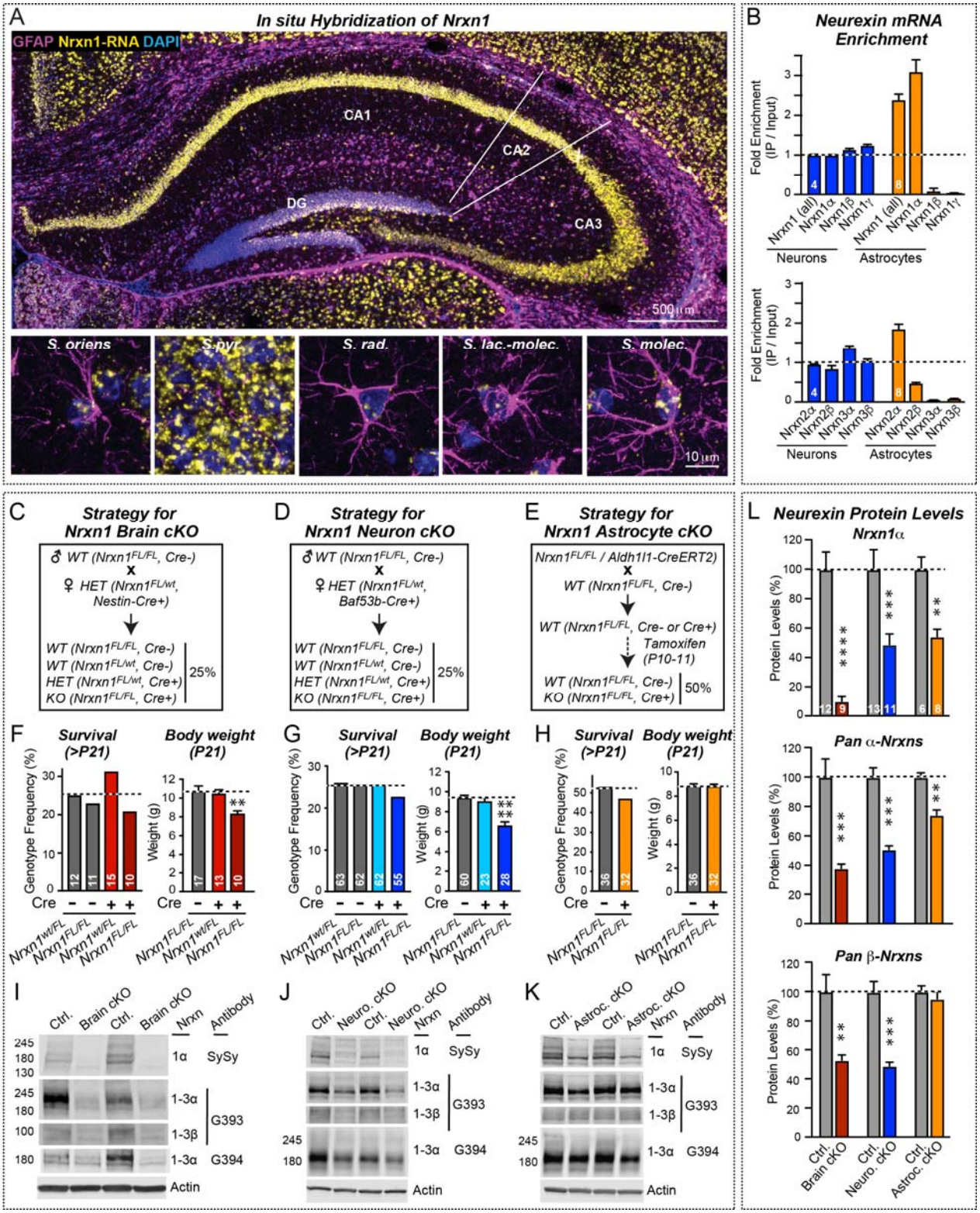

Figure 1: **Astrocytes express high levels of Nrxn1α equivalent to neurons**

(A) Single-molecule *in situ* hybridization reveals Nrxn1 expression in neurons and astrocytes of the hippocampus. Representative images show hippocampal section from young adult mouse (P30) labeled by *in situ* hybridization for Nrxn1 (yellow), by immunocytochemistry for GFAP (purple), and by DAPI for nuclei (blue). Top, overview; bottom, expanded images of layer specific astrocytes in the CA1 and DG regions (from left to right, Stratum oriens, pyramidale, radiatum, and lacunosome-moleculare of the CA1 region; S. moleculare of the DG).

(B) Neurexin mRNA quantifications demonstrate high-level expression of Nrxn1α and Nrxn2α, but not of other neurexin isoforms, in astrocytes. Summary graphs depict the relative enrichment of the indicated neurexin mRNAs in neurons or astrocytes as compared to the total brain. Neurexin mRNA levels were determined by quantitative RT-PCR in total homogenates and in astrocyte- or neuron-specific ribosome-bound mRNAs that were isolated from RiboTag mice crossed with neuron- or astrocyte-specific Cre-driver lines (Fig. S2D; all samples were from mouse hippocampus at P26-P30). Note that the data do not allow comparison of astrocytic vs. neuronal mRNA levels, but only of mRNA levels within a cell type.

(C-E) Breeding strategies of brain- (C), neuron- (D), and astrocyte-specific (E) Nrxn1 cKOs. Breeding strategies operate with classical Nrxn1 cKO mice (Chen et al., 2017) or with Nrxn1 conditional HA-knockin mice (Trotter et al., 2019; Fig. S3). All functional experiments were performed with classical cKO mice, while conditional HA-knockin mice were only used for localization and modification studies of Nrxn1.

(F-H) Brain- (F), neuron- (G), and astrocyte-specific (H) Nrxn1 deletions do not alter mouse survival (left graphs) but the brain- and neuron-specific Nrxn1 deletions decrease mouse weight at weaning (right graphs).

(I-K) Representative immunoblots (top) and quantifications of neurexin levels (bottom) in total brain samples from brain- (I), neuron- (J), and astrocyte-specific (K) Nrxn1 cKO and littermate control mice. Blots used different neurexin antibodies that mostly recognize multiple neurexin isoforms.

(L) Astrocytes and neurons each contribute approximately 50% to the brain's Nrxn1α protein. Summary graphs show relative protein levels quantified in hippocampal homogenates of Nrxn1 cKO mice that were crossed with the indicated Cre-driver mice (antibodies used for quantifications: Nrxn1α, SySy; pan-α-Nrxns, G393; pan-β-Nrxns, G393; see Fig. S2E for details).

Numerical data are means ± SEM (numbers of mice are shown in graphs; for astrocyte mRNAs (B), samples from 2 mice each were pooled). Statistical significance was assessed with a chi²-test (F-H, survival), one-way ANOVA with a Tukey's post-hoc test (F-H, body weight), and two-tailed unpaired t-test comparing test to control samples (L), with * = $p < 0.05$; ** = $p < 0.01$; *** = $p < 0.001$, **** = $p < 0.0001$.

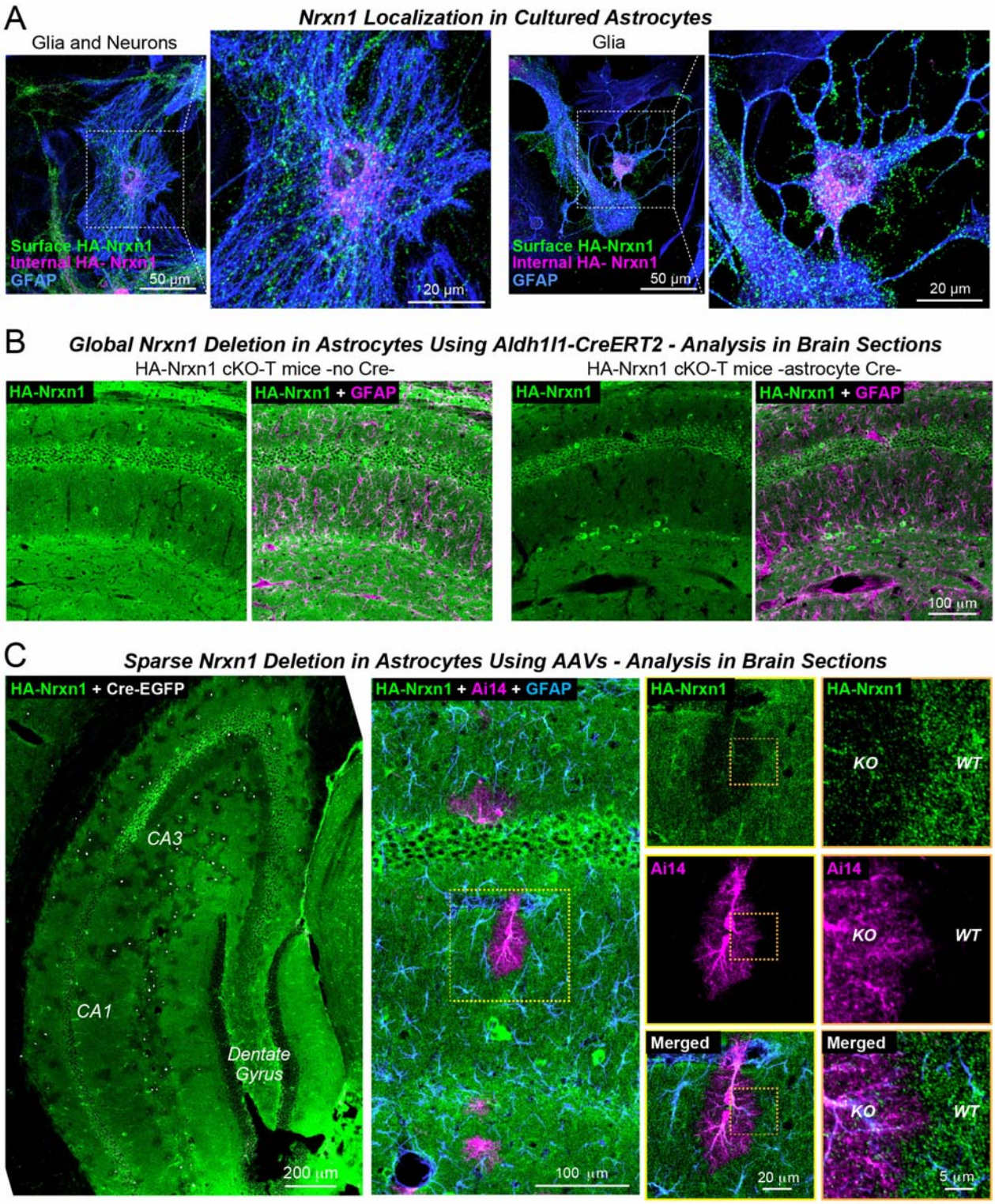

Figure 2: **Nrxn1α is abundantly expressed on the surface of astrocytes and is transported to fine astrocytic processes in the neuropil of the hippocampus**

(A) Nrxn1α is clustered on the surface of astrocytes cultured from Nrxn1 HA-knockin mice. Surface (green) and internal HA-Nrxn1 (red) were visualized by immunocytochemistry for HA

before or after permeabilization, respectively, in mixed neuron-glia cultures (left) or in pure glia cultures (right). Cells were analyzed at DIV14 and also stained for GFAP (blue) as an astrocyte marker.

(B) Astrocytes contribute to the total HA-Nrxn1 staining in the neuropil of the CA1 region as evidenced by astrocyte-specific deletion of HA-Nrxn1. HA-Nrxn1 HA-knockin mice crossed with Aldh1l1-CreERT2 mice were injected with tamoxifen at P10-P11, and analyzed by immunocytochemistry at P26-30 (green, HA-Nrxn1; magenta GFAP).

(C) Sparse Cre-mediated deletion of HA-Nrxn1 in astrocytes documents the contribution of astrocytic Nrxn1 to neuropil's overall expression of Nrxn1. HA-Nrxn1 cKO mice crossed with Ai14 reporter mice were minimally injected at P2-P3 with AAVs expressing Cre-eGFP from a GFAP promoter and analyzed at P26-P30 (left, hippocampus overview section stained for HA-Nrxn1 (green) and Cre-eGFP (white); middle, CA1 region overview imaged for HA-Nrxn1 (green), GFAP (blue), and tdTomato (red, expression activated by Cre in Ai14 reporter mice); middle right panels, enlarged images from the boxed area in the middle picture to illustrate individual HA-Nrxn1 and tdTomato signal; extreme right panels, enlarged images from the boxed area in the middle middle right panels to further illuminate precise localization of astrocytic HA-Nrxn1).

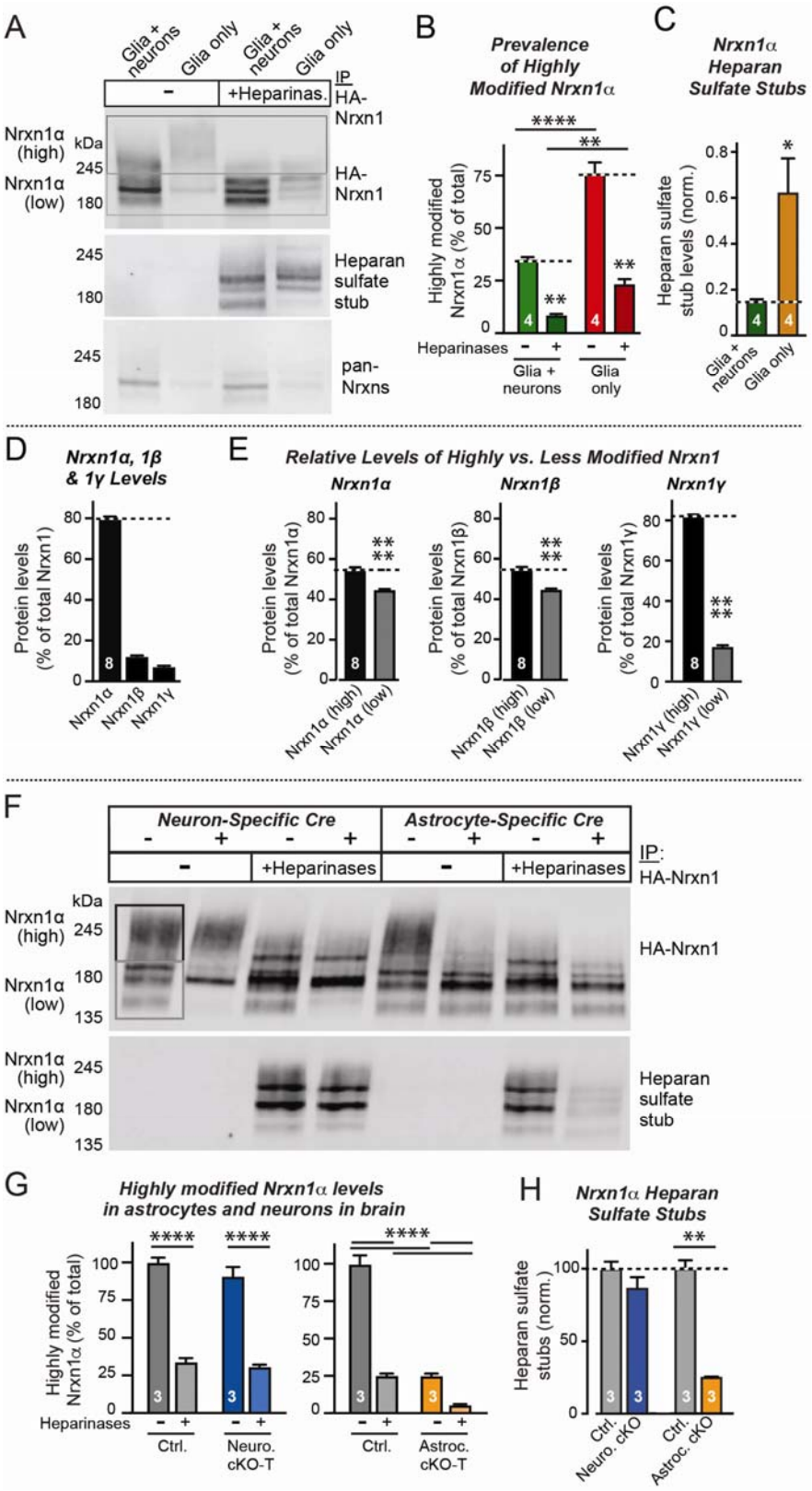

Figure 3: **Nrxn1α is expressed as a heparan sulfate proteoglycan in astrocytes but not in neurons**

(A-C) Nrxn1α is expressed primarily as a heparan sulfate proteoglycan in cultured astrocytes but not cultured neurons. Nrxn1 was immunoprecipitated at DIV14-16 from mixed neuron-glia cultures or pure glia cultures obtained from Nrxn1 HA-knockin mice. Immunoprecipitates were analyzed by immunoblotting without or with heparinase treatment that cleaves heparan sulfate modifications, exposing a heparan sulfate stub that can be visualized by an antibody (A, representative immunoblots; B & C, relative abundance of highly-modified vs. less-modified Nrxn1α (B), or of Nrxn1α heparan-sulfate stubs (C)). In the mixed cultures, the relative amounts of highly modified Nrxn1α are decreased relative to the pure glia cultures presumably because more neuronal Nrxn1α is not highly modified.

(**D & E**) Quantification of the total relative amounts of Nrxn1α protein, Nrxn1β protein, and Nrxn1γ protein in brain (D) and of the relative amounts of highly and less modified forms of Nrxn1α, Nrxn1β, and Nrxn1γ (for sample immunoblots and further quantifications, see Fig. S3B-S3D).

(F-H) In vivo, Nrxn1α is present in astrocytes primarily as a heparan-sulfate proteoglycan, whereas Nrxn1α in neurons largely lacks heparan-sulfate modification. Brain lysates from the control mice or mice with astrocyte- or neuron-specific HA-Nrxn1 deletions were examined by Nrxn1 immunoprecipitation, followed by immunoblotting without or with heparinase treatment (F, representative immunoblots for Nrxn1a (top) and heparan-sulfate stubs (bottom); G & H, summary graphs of the relative abundance of highly vs. less modified Nrxn1α (G) or of Nrxn1α heparan-sulfate stubs normalized to total Nrxn1α levels (H).

Numerical data are means ± SEM (numbers of mice or cultures are shown in graphs). Statistical significance was assessed with a two-way ANOVA with Tukey's post-hoc test (B, G, H) or with a two-tailed unpaired t-test to controls (rest of graphs), with * = $p < 0.05$; ** = $p < 0.01$; *** = $p < 0.001$; **** = $p < 0.0001$.

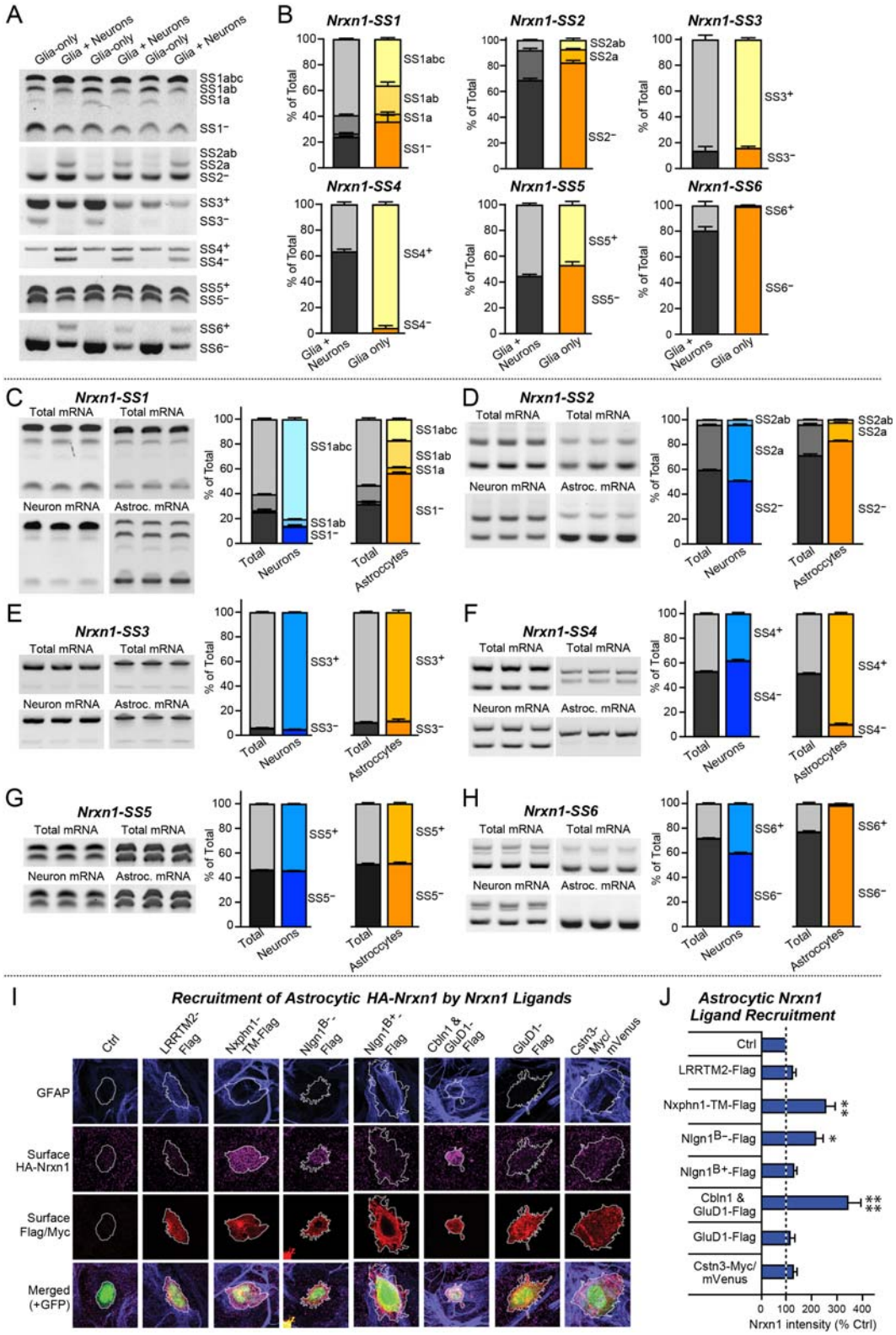

Figure 4: **Nrxn1 alternative splicing differs between astrocytes and neurons, limiting the range of ligands that can be engaged by astrocytic Nrxn1**

(A & B) RT-PCR analysis of Nrxn1 alternative splicing using mRNA from mixed glia-neuron cultures or from pure glia cultures (primarily astrocytes), both prepared from the hippocampus of newborn mice and examined at DIV14-DIV16. In glia, Nrxn1 mRNAs nearly always contain an insert in splice site #4 (SS4) and lack an insert in SS2 and SS6, whereas mixed cultures express a mixture of *Nrxn1* splice variants (left, representative gel images; right, summary graphs of individual splice sites).

(C-H) RT-PCR analysis of Nrxn1 alternative splicing using mRNA isolated from mouse hippocampus at P26-P30. Comparison of Nrxn1 alternative splicing at SS1 to SS6 in neurons vs. astrocytes reveals profound differences. Translating mRNAs were immunoprecipitated from neurons or astrocytes using Cre-dependent RiboTag mice crossed with neuron- or astrocyte-specific Cre-driver mice (described in 1B, S2D). Similar to A, junction-flanking RT-PCR was used to amplify and quantify alternative splice variants. Each panel depicts a single site of alternative splicing (left, representative gel images; right, distribution of splice variants in % of total).

(I & **J)** Only a subset of Nrxn1 ligands when expressed in HEK293T cells recruit HA-Nrxn1 expressed on co-cultured astrocytes. Pure cultures of glia were co-cultured with HEK293T cells expressing the indicated Nrxn1 ligands. After 48 h, HA-Nrxn1 recruitment to GFAP-positive astrocytes was quantified (I, representative images; J, quantification of HA-Nrxn1 recruitment).

Numerical data are means ± SEM (for A-B, n = 3 independent cultures; for C-H, n = 4 mice for neuron mRNAs and 8 mice with 2 mice pooled per pull-down for astrocyte mRNAs; for I-J, 10-20 cells averaged per culture from 3-6 cultures). Statistical significance was assessed with a two-tailed unpaired t-test to controls (J), with * = $p < 0.05$; ** = $p < 0.01$; **** = $p < 0.0001$.

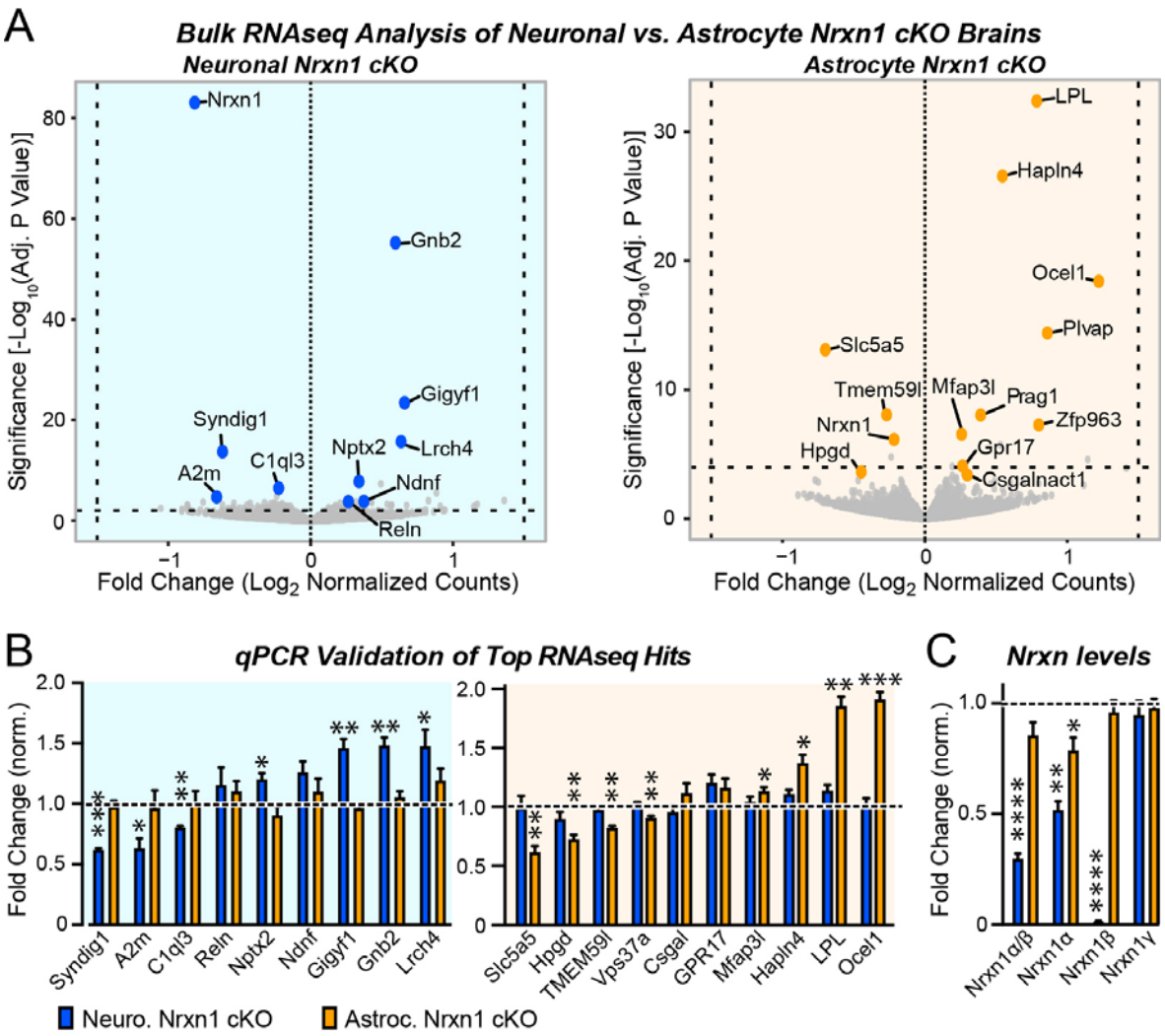

Figure 5: **RNAseq reveals that neuronal and astrocytic Nrxn1 control distinct transcription programs in the hippocampus**

(A) Volcano plots of batch-normalized differential gene expression in the hippocampus of neuron- (left) and astrocyte-specific Nrxn1 cKOs (right). Bulk RNAseq analysis was performed at P26 in two batches with two control and two cKO mice (2 males and 2 females).

(B) Quantitative RT-PCR validation of top differentially expressed genes emerging from RNAseq experiments (left, neuron-specific cKO; right, astrocyte-specific cKO; n = 4 per genotype).

(C) Quantitative RT-PCR measurements of the mRNA levels of the major Nrxn1 isoforms using the samples analyzed by bulk RNAseq.

Data in B and C are means ± SEM. Statistical significance was assessed with a two-tailed unpaired t-test to controls (B and C; for statistical analysis of RNAseq data, see Experimental Procedures), with * = $p < 0.05$; ** = $p < 0.01$; *** = $p < 0.001$; **** = $p < 0.0001$.

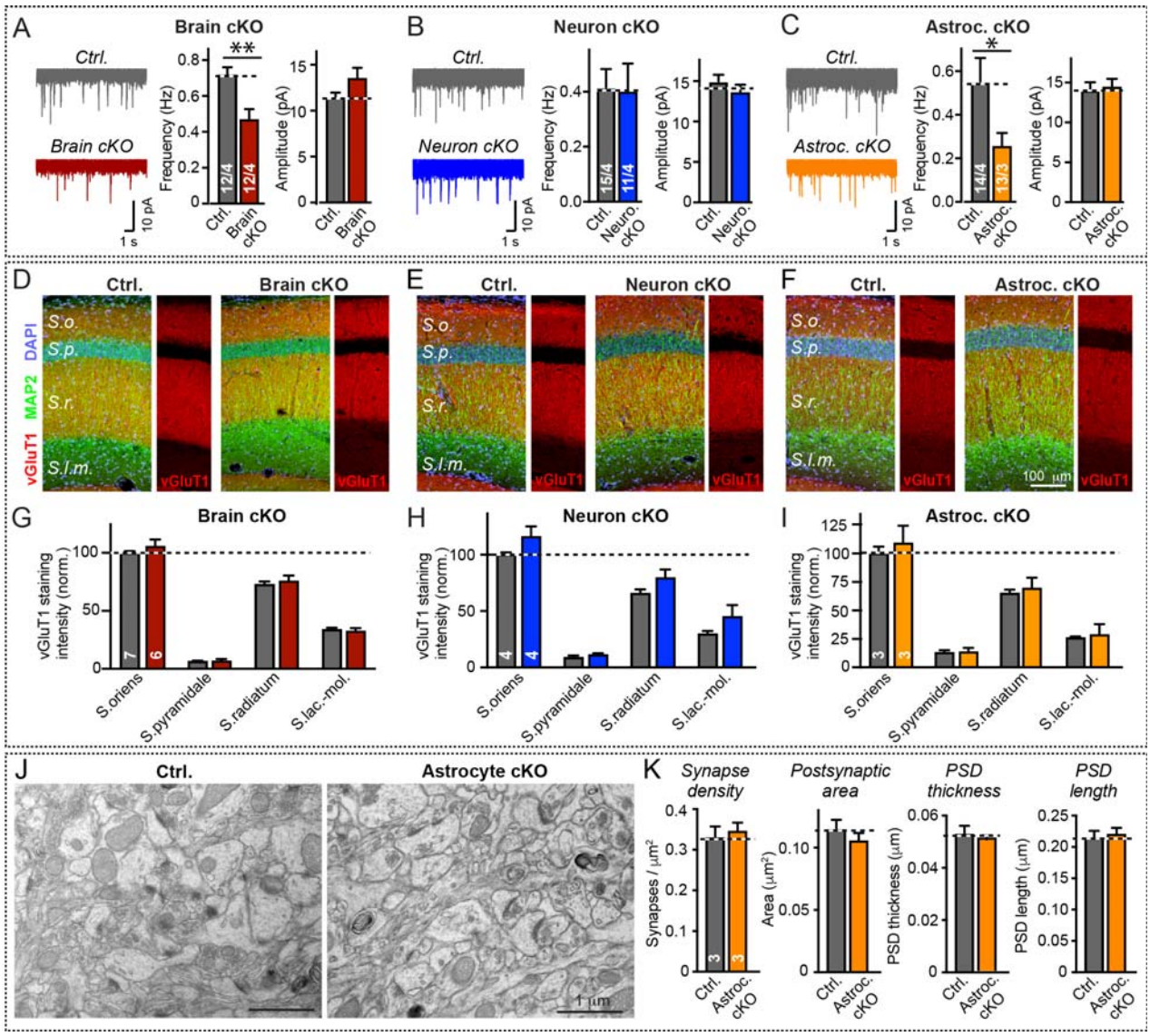

Figure 6: **Deletion of Nrxn1 from astrocytes suppresses spontaneous excitatory synaptic transmission without altering synapse numbers or synapse structure**

(A-C) Astrocyte- but not neuron-specific deletion of Nrxn1 in cKO mice reduces the mEPSC frequency without changing the mEPSC amplitude. mEPSCs were recorded at P22-P26 in acute slices from CA1 pyramidal neurons prepared from brain- (A), neuron- (B), and astrocyte-specific Nrxn1 cKOs (C). Representative traces are shown to the left of summary graphs of the mEPSC frequency (middle) and amplitude (right).

(D-F) Representative sections of the hippocampal CA1 region from control mice and mice with brain- (D), neuron- (E), or astrocyte-specific deletion of Nrxn1 (F) were stained for the excitatory presynaptic marker vGluT1 (red), the dendritic marker MAP2 (green), and the nuclear marker DAPI (blue). Smaller panels to the right of main panels show only vGluT1 staining as a proxy for synapse density (S.o., Stratum oriens; S.p., Stratum pyramidale; S.r., Stratum radiatum; S.l.m., Stratum lacunosum-moleculare).

(G-I) Deletion of Nrxn1 from the whole brain (G) or from only neurons (H) or astrocytes (I) has no effect on excitatory synapse density in hippocampal area CA1 at P26-P30. Summary graphs quantify the vGluT1 staining intensity (normalized to that of MAP2 and expressed as % of S. oriens levels) for the indicated layers.

(J & **K)** Electron microscopy reveals that deletion of Nrxn1 from astrocytes does not alter excitatory synapse density or synapse structure in the S. radiatum of the CA1 region (J, representative electron micrographs of the neuropil; K, summary graphs of synapse density, postsynaptic area, PSD thickness, and PSD length).

Numerical data are means ± SEM (number of cells/slices [A-C] or mice [G-I, K] are shown in bar graphs). Statistical significance was determined by two-tailed Mann Whitney test (A-C) or two-tailed unpaired t-test to controls (G-I, K), with * = $p < 0.05$; ** = $p < 0.01$.

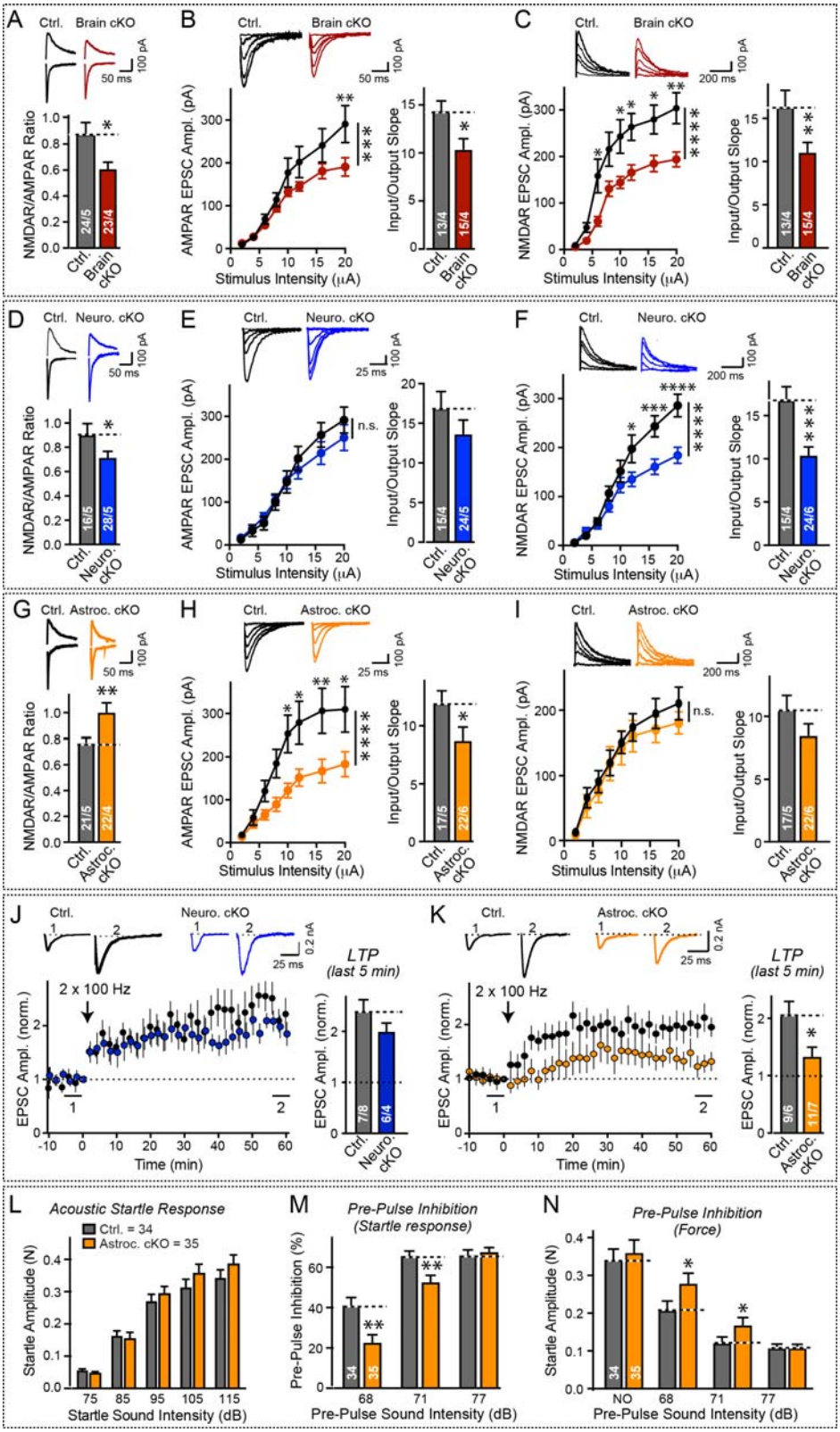

Figure 7: **Neuronal and astrocytic Nrxn1 perform non-overlapping functions in regulating excitatory synaptic transmission and long-term synaptic plasticity**

(A-C) Deletion of Nrxn1 from the entire brain decreases the NMDAR/AMPAR ratio (A) and the amplitudes of evoked AMPAR- (B) and NMDAR-EPSCs (C). EPSCs evoked by electrical stimulation of Schaffer collaterals were recorded from hippocampal CA1 pyramidal neurons in acute slices from P22-P26 mice of the indicated genotypes. AMPAR-EPSCs were recorded as the peak amplitude with a -70 mV holding potential, and NMDAR-EPSCs as the amplitude at 50 ms after the stimulus with a +40 mV holding potential. Sample traces are shown on top; for B and C, input-output curves (left) and slopes (right) are depicted separately.

(D-F) Neuron-specific deletion of Nrxn1 also lowers the NMDAR/AMPAR ratio (D) but has no effect on the AMPAR-EPSC amplitude, while it still decreases the strength of evoked NMDAR-EPSCs (F). Experiments were performed as in A-C.

(G-I) Astrocyte-specific deletion of Nrxn1 increases instead of decreasing the NMDAR/AMPAR ratio (G) and suppresses AMPAR-EPSCs (H) but has no effect on NMDAR-ESPCs (I). Experiments were performed as in A-C.

(J & **K)** Neuron-specific deletion of Nrxn1 does not significantly affect the induction of NMDAR-dependent LTP (J), whereas the astrocyte-specific deletion of Nrxn1 severely impairs LTP (K). Schaffer-collateral LTP was induced by two 100-Hz/1s stimulus trains separated by a 10 s interval, and recorded from CA1 pyramidal neurons (top, sample traces; bottom left, summary plot of LTP time course; bottom right, LTP amplitude during the last 5 min of recording).

(L-N) Astrocyte-specific deletion of Nrxn1 impairs pre-pulse inhibition of the acoustic startle response without altering the startle response itself (L, measurements of the startle response elicited by acoustic stimuli of 75 - 115 dB; M, pre-pulse inhibition of the startle response amplitude in response to acoustic stimuli of 115 dB preceded by pre-pulses of 68, 71, and 77 dB; N, same as M, but monitored as the force of the startle response).

All data are means ± SEM (numbers in bars represent number of cells / mice tested (A-K) or number of mice tested (L-N)). Statistical analysis was assessed by two-way ANOVA with Sidak's multiple comparison test (all input-output plots), two-tailed unpaired t-test (A, D, G, J & K, and all input-out-output slopes), and repeated-measures ANOVAs with the between-subject factors genotype and sex and the within-subject factor startle sound intensity or pre-pulse sound intensity (L-N), followed by two-tailed unpaired t-tests when appropriate (* = $p < 0.05$; ** = $p < 0.01$; *** = $p < 0.001$; **** = $p < 0.0001$).